Exploring the pathogenic role of tertiary lymphoid structures in chronic blisters of patients with pemphigus

A Yeong Lee

The Graduate School
Yonsei University
Department of Medicine

Exploring the pathogenic role of tertiary lymphoid structures in chronic blisters of patients with pemphigus

A Dissertation Submitted
to the Department of Medicine
and the Graduate School of Yonsei University
in partial fulfillment of the
requirements for the degree of
Doctor of Philosophy in Medical Science

A Yeong Lee

December 2024

This certifies that the Dissertation of A Yeong Lee is approved

Thesis Supervisor	Jong Hoon Kim
Thesis Committee Member	Do-Young Kim
Thesis Committee Member	Eui-Cheol Shin
Thesis Committee Member	Sang-Jun Ha
Thesis Committee Member	Ho-Keun Kwon

The Graduate School
Yonsei University
December 2024

ACKNOWLEDGEMENTS

I would like to express my deepest and most sincere gratitude to my advisor, Professor Jong hoon Kim, for his invaluable guidance, profound insight, and unwavering support throughout every stage of my doctoral studies. His mentorship has not only been instrumental in shaping the course of my research but has also profoundly influenced my development as a scholar and as an individual. Professor Kim's dedication to his students and his commitment to fostering an environment of intellectual curiosity have inspired me to approach my academic work with unwavering rigor and passion. I am truly honored to have been his student, and I am grateful beyond words for his belief in me and his encouragement, which have sustained me through challenges and accomplishments alike.

I am also profoundly grateful to my esteemed dissertation committee members—Professors Do-Young Kim, Eui-Cheol Shin, Sang-Jun Ha, and Ho-Keun Kwon—who generously offered their time, expertise, and thoughtful guidance. Their valuable advice, constructive feedback, and continuous encouragement throughout the course of this work have greatly enriched my academic journey and have been pivotal in refining and elevating my research. Each of them brought unique insights that helped me navigate complex questions and clarify my contributions to the field. Their commitment to excellence has been both humbling and inspiring, and I am deeply appreciative of their support.

Special thanks are due to the research members of the Dermatology Laboratory—Dawoon Han and Taehee Kim, who actively contributed as co-authors of this dissertation and provided invaluable assistance and guidance throughout my research. I am deeply grateful for their significant role in shaping this work. I also extend my heartfelt gratitude to Seoyeon Min and Song-Ee Kim, whose unwavering support and dedication played a critical role in advancing my research. Working alongside such skilled and compassionate individuals has been a privilege, and I am incredibly thankful for the collaborative spirit and encouragement they fostered in our lab.

Finally, I owe my deepest and most heartfelt appreciation to my husband, Yechan Kim. His constant care, encouragement, and unfailing support have made it possible for me to complete this journey. Yechan has been my pillar of strength, offering comfort and motivation through every high and low, and his steadfast presence has given me the resilience to persevere. I am also deeply thankful to my family, whose love, understanding, and encouragement have always been a source of strength for me. I am beyond words in expressing my gratitude for his patience, understanding, and sacrifices, all of which have made this achievement possible. This milestone is as much his as it is mine, and I am eternally thankful to have him by my side.

To everyone who accompanied me on this journey, my gratitude knows no bounds. Thank you for believing in me, guiding me, and inspiring me to reach this moment.

TABLE OF CONTENTS

LIST OF FIGURES

LIST OF TABLES

ABSTRACT

Exploring the pathogenic role of tertiary lymphoid structures in chronic blisters of patients with pemphigus

Pemphigus is a rare and life-threatening autoimmune blistering disease mediated by autoreactive B cells targeting desmogleins (DSGs) in keratinocytes. Anti-DSG autoantibodies disrupt cell-cell adhesion, leading to suprabasal acantholytic blisters. Disease control is achieved using systemic medications such as rituximab and high-dose systemic corticosteroids with immunosuppressants. However, some patients may continue to experience chronically recurring blistering lesions on a specific site for several months or more, necessitating long-term systemic therapy. Our investigation reveals the presence of tertiary lymphoid structures (TLSs) harboring DSG-specific B cells and plasma cells in chronic skin blisters of patients with pemphigus. These TLSs, resembling B-cell follicles of secondary lymphoid organs (SLOs), are detected in various inflammatory diseases. TLSs have high expression of CXCL13, a crucial chemokine responsible for recruiting CXCR5-expressing naïve B and T follicular helper cells. However, the expansion and functional regulation of CXCL13-secreting cells within TLSs remain unclear. In the skin TLSs, $CD4^+$ T cells are the primary producer of CXCL13. Single-cell RNA sequencing revealed clonally expanded $CXCL13^+CD4^+$ T cells containing DSG3-specific memory T cells with activated cytotoxic features. Paradoxically, these cells exhibit an attenuation of T-cell receptor (TCR) signaling when expressing high levels of *CXCL13*. Using a highly multiplex imaging technique called CO-Detection by indEXing (CODEX), spatial proteomics reveals direct interactions between regulatory T cells (Tregs) and $CXCL13^+CD4^+$ T cells. In vitro depletion of Tregs results in decreased CXCL13 production by $CD4^+$ T cells. Notably, intralesional corticosteroid injection leads to the disappearance of TLSs and chronic blisters. In this study, skin TLSs are associated with the persistence of chronic blisters in pemphigus, and the microenvironmental network of Tregs and $CXCL13^+CD4^+$ T cells is crucial for TLS formation.

Key words : pemphigus, autoimmune bullous disease, tertiary lymphoid structure, chronic blister, pathogenicity, rituximab, $CD4^+$ T cells, B cells

1. INTRODUCTION

Pemphigus is a rare and life-threatening autoimmune disease that manifests as blisters and erosions on skin and/or mucosa. It is mediated by autoreactive B cells targeting desmoglein 1 (DSG1) and/or DSG3, the transmembrane binding proteins of desmosomes in keratinocytes. Anti-DSG autoantibodies cause a loss of cell-cell adhesion in keratinocytes, leading to blistering at mucocutaneous sites[1]. Pemphigus is classified as pemphigus vulgaris (PV), pemphigus foliaceus (PF), or paraneoplastic pemphigus (PNP). PV induced by anti-DSG3 autoantibody mainly affects the oral mucosa, whereas PF induced by anti-DSG1 autoantibody presents as superficial blisters on the skin. PNP is known as one of the paraneoplastic autoimmune diseases caused by underlying neoplasms[2]. Autoreactive B cells producing anti-DSG IgG are pathogenic in pemphigus. Anti-DSG3 IgG autoantibodies positively correlate with disease activity, and pathogenic monoclonal antibodies from pemphigus are necessary and sufficient to cause acantholytic blisters[3].

Rituximab is a monoclonal anti-CD20 antibody that targets $CD20^+$ B cells. Meta-analyses have supported the remarkable efficacy of rituximab in pemphigus, with 59–100% of patients achieving complete clinical remission after treatment. Rituximab shows partial or complete remission achieved 3 to 6 months after rituximab treatment in 75% of patients with pemphigus, thus currently used as early administration of rituximab shortens the time to remission[4-6]. Following disease control achieved using systemic medications such as rituximab and high-dose systemic corticosteroids with immunosuppressants, treatment can be maintained with low-dose systemic corticosteroids, low-dose immunosuppressants, or no treatment at all[7]. However, even with the treatment, some patients may continue to experience chronically recurring blistering lesions on a specific site for several months or more. These lesions, referred to as chronic blisters in this study, rarely disappear despite prolonged use of maintenance systemic treatment. As a result, affected patients may require long-term systemic drug therapy to achieve complete remission.

Tertiary lymphoid structures (TLSs) are organized aggregates of immune cells such as T and B cells that arise postnatally in nonlymphoid tissue. TLSs are not present under physiological conditions but form in chronically inflamed environments, for instance, in cancer, infection, chronic inflammation, allograft rejection, and autoimmune disease. TLSs are characterized by an inner zone of $CD20^+$ B cells that is surrounded by $CD3^+$ T cells, similar to the B cell follicles in secondary lymphoid organs (SLOs) including the spleen and lymph nodes[8]. TLSs can vary in their specific composition, but within the T cell compartment, they typically include $CD4^+$ T follicular helper (Tfh) cells, $CD4^+$ T helper (Th) cells, $CD8^+$ cytotoxic T cells, and regulatory T cells (Tregs). Additionally, follicular dendritic cells (FDCs), which originate from mesenchymal cells, are present and play a critical role in selecting memory B cells during germinal center (GC) reactions in secondary lymphoid organs (SLOs). Lastly, peripheral node addressin (PNAd)–positive high endothelial

venules (HEVs) provide the specialized vasculature associated with TLSs that is thought to mediate lymphocyte recruitment[8, 9]. The clinical contribution of TLSs to diseases has garnered attention owing to the association of TLSs with a favorable response to immune checkpoint inhibitors in cancer tissues[10-12]. In addition to cancers, autoreactive B cells capable of perpetuating autoimmune responses have been detected in TLSs of autoimmune diseases, such as rheumatoid arthritis and autoimmune thyroid diseases[13, 14]. TLSs has been found to correlate with serum autoantibody concentrations, disease severity, and decreased organ function in several autoimmune diseases, including Sjögren's syndrome, myasthenia gravis, and Hashimoto's thyroiditis, suggesting a potential contribution of TLSs to disease progression[15, 16].

TLSs have high expression of CXCL13, a chemokine responsible for the recruitment of CXCR5-expressing immune cells, such as naive B cells and T follicular helper (Tfh) cells[17]. CXCL13 has been specifically associated with TLS development. Ectopic CXCL13 expression is sufficient for recruiting B cells and inducing TLS formation in nonlymphoid tissues. Although CXCL13 is commonly known as a chemokine produced by follicular dendritic cells in human SLOs and mice, CXCL13-producing T cells have been found in inflamed human tissues[18]. Moreover, these $CXCL13^+$ T cells are located in TLSs and contribute to their formation[19]. Enrichment of $CXCL13^+$ T cells predict favorable outcomes to immunotherapy, indicating that T cells play a crucial role as CXCL13-producing cells[20]. However, how $CXCL13^+$ T cells are expanded and functionally regulated within TLSs is not yet known.

Here, we investigated TLSs containing DSG-specific B cells and plasma cells in chronic blisters from patients with pemphigus. We demonstrate upregulation of CXCL13, which is mainly produced by $CD4^+$ T cells, in skin samples with TLSs. We also show that $CXCL13^+CD4^+$ T cells are clonally expanded. These $CXCL13^+CD4^+$ T cells are characterized by activated Th1-like $CD4^+$ T cells, but paradoxically downregulated genes associated with T cell receptor (TCR) signaling when they had high expression of *CXCL13*. By using a highly multiplex imaging technique, we found that Tregs directly contact $CXCL13^+CD4^+$ T cells and promote the production of CXCL13 in $CD4^+$ T cells. Finally, we report the decrease of TLSs and chronic blisters in patients with pemphigus after intralesional injection of corticosteroid. In conclusion, skin TLSs are associated with the maintenance of chronic blister in patients with pemphigus, and the microenvironmental network between clonal $CXCL13^+CD4^+$ T cells and Tregs is important for production of CXCL13 in the TLSs.

2. MATERIALS AND METHOD

2.1. Patients

A total of 41 patients with pemphigus were enrolled in the study (NCT04509570). A total of 10 patients were enrolled in a retrospective study, while 31 patients with pemphigus with chronic blisters were enrolled in a prospective study, including 18 who were treated with intralesional corticosteroids after the presence of skin TLSs in the lesions was confirmed. The time period was established by obtaining a detailed patient history. Regarding cases of recurrence, lesion duration was defined as the period after by rituximab treatment of the last recurrence. Triamcinolone (10 mg/mL) was used each month until the lesions disappeared. Numbers of treatments varied in patients, and treatment was stopped when patients refused continuation of treatment or experienced relapse. Changes in the skin lesions were calculated using ImageJ (NIH).

2.2. Immunohistochemistry

For immunohistochemical staining, paraffin-embedded tissues were obtained from Human Tissue Bank of Gangnam Severance Hospital, Yonsei University College of Medicine, and were sectioned (5 μm) and stained with primary antibodies: rabbit anti-human CD138 (EP201), rabbit anti-human CD4 (SP35), rabbit anti-human CD11c (EP157), and mouse anti-human podoplanin (D2-40) (all from Cell Marque); mouse anti-human CD20 (L26) and rabbit anti-human lymphotoxin β (both from Abcam); mouse anti-human FDC (CAN.42, Thermo Fisher Scientific); and rat anti-human PNAd (MECA-79, BioLegend).

2.3. Immunofluorescence

Fresh tissues were obtained from the patients via 4–6 mm punch biopsy. Half of the tissues were fixed in 1% paraformaldehyde for 4 hours at room temperature and incubated in 20% sucrose overnight at 4°C. The tissues were sectioned (4 μm) and permeabilized with 0.5% Triton X-100 for 30 minutes. After washing with PBS, the slides were incubated in blocking solution (X0909, DAKO) for 1 hour. Tissues were stained overnight at 4°C using the following primary antibodies: mouse anti-human CD20 (L26, Abcam); 6X His-recombinant human DSG1 and 6X His-recombinant human DSG3 (both from Cusabio); goat anti-human CXCL13 (R&D Systems); rabbit anti-human CCL5 (P230E, Thermo Fisher Scientific); rabbit anti-human CD138 (EP201),

rabbit anti-human FDC (CNA.42), and mouse anti-human CD8 (C8/144B) (all from Cell Marque); rat anti-human CD4 (YNB 46.1.8, Santa Cruz); and mouse anti-human HLA-DR (L243, BioLegend). Tissues were washed with PBS and incubated for 1 hour at room temperature with secondary antibody: Alexa Flour 488–conjugated goat anti-mouse and anti-rat antibodies; Alexa Flour 594–conjugated goat anti-rabbit, anti-mouse, and anti-rat antibodies; Alexa Flour 647–conjugated goat anti-mouse and anti-rat antibodies (all from Invitrogen); donkey anti-goat antibody (Jackson ImmunoResearch); and mouse anti-6X His-tag antibody (R&D Systems). Nuclei were stained with DAPI (Thermo Fisher Scientific). Fluorescence images were captured on an LSM 780 confocal microscope (Carl Zeiss).

2.4. In vitro culture of CXCL13-producing $CD4^+$ T cells

PBMCs from healthy volunteers were separated by standard Ficoll-Paque (GE Healthcare) density gradient centrifugation. $CD4^+$ T cells were isolated by MACS using a human $CD4^+$ T cell isolation kit (Miltenyi Biotec) according to the manufacturer's protocol. Isolated $CD4^+$ T cells were differentiated at 37°C in a 5% CO2 atmosphere for 5 days in IMDM (Thermo Fisher Scientific) containing 10% fetal bovine serum (Welgene) and 100 units/mL penicillin and streptomycin (Thermo Fisher Scientific). For the depletion of Tregs, $CD4^+$ T cells were stained for 10 minutes at room temperature using PerCP-Cy5.5–conjugated anti-CD4 (RPA-T4), PE-Cy7–conjugated anti-CD127 (A019D5), and APC-conjugated anti-CD25 (BC96) (all from BioLegend) and sorted by FACS Aria III (BD Biosciences) into $CD25^+CD127^{lo}CD4^+$ Tregs and other $CD4^+$ T cells. Tregs were labeled with Cell Trace Violet (Invitrogen) and other $CD4^+$ T cells were labeled with Cell Trace Far Red (Invitrogen). To generate CXCL13-producing $CD4^+$ T cells, cells were stimulated with plate-coated 5 μg/mL anti-CD3 (OKT3, Invitrogen) and soluble 10 μg/mL anti-CD28 (CD28.2, BD Biosciences) antibodies in the presence of 2 ng/mL TGF-β1 (Cell Signaling Technology), 10 ng/mL IL-6 (Peprotech), and 10 μg/mL neutralizing anti–IL-2 antibody (R&D Systems). To generate iTregs (>95% of $CD4^+$ T cells), $CD25^-CD4^+$ naive T cells were cultured in 96-well plates coated with 5 μg/mL anti-CD3 (OKT3, Invitrogen) and soluble 10 μg/mL anti-CD28 (CD28.2, BD Biosciences) antibodies and stimulated with 5 ng/mL TGF-β1 (Cell Signaling Technology) and 50 U/mL IL-2 (Peprotech) in 10% IMDM (Thermo Fisher Scientific) for 5 days. After 5 days, For the coculture system of $CXCL13^+CD4^+$ T cells and iTregs, presorted $CD4^+$ T cells were stained with the following antibodies: FITC-conjugated anti-CCR7 (G043H7), PerCP-Cy5.5–conjugated anti-CD4 (RPA-T4), PE-Cy7–conjugated anti-CD45RA (HI100), and PE-CF594–conjugated anti-CD25 (BC96) (all from BioLegend) and APC-conjugated anti-CD127 (HIL-7R-M21) (BD Biosciences). Then, they were sorted using a FACS Aria III into $CCR7^+CD45RA^+CD25^-$ naive $CD4^+$ T cells and other $CD25^-CD4^+$ Tm cells. $CD25^-CD4^+$ Tm cells were used for differentiation of CXCL13-producing $CD4^+$ T cells. CXCL13-producing $CD4^+$ T cells (400,000/well) were mixed with iTregs at a 2:1

ratio for 24 hours in 10% IMDM (Thermo Fisher Scientific) with or without 50 U/mL IL-2 (Peprotech) and 10 μg/mL neutralizing anti–TGF-β1 antibody (R&D Systems). To stain CXCL13-producing $CD4^+$ T cells, monensin (BD Biosciences) was added during the last 5 hours of coculture. To assess cytokine secretion, CXCL13-producing $CD4^+$ T cells were stimulated with 50 ng/mL PMA and 1 μg/mL ionomycin. After 1 hour, cells were treated with monensin for 5 hours. Cells were harvested and stained with the following antibodies: BV510-conjugated anti-CD3 (UCHT1), APC-conjugated anti-CD127 (HIL-7R-M21) (both from BD Bioscience), PerCP-Cy5.5–conjugated anti-CD4 (RPA-T4), FITC-conjugated anti-GITR (108-17), and PE-CF594–conjugated anti-CD25 (BC96) (all from BioLegend). Dead cells were excluded using the LIVE/DEAD Fixable Red or Near-IR Cell Stain Kit (Invitrogen). For intracellular staining, the cells were fixed and permeabilized using the Foxp3/Transcription Factor Staining Buffer Set (Invitrogen). After permeabilization, cells were incubated for 30 minutes at 4°C with PE-conjugated anti-CXCL13 (IC801P, R&D Systems), BV605-conjugated anti–TNF-α (Mab11, BioLegend), BV711-conjugated anti–IFN-γ (B27), and BV786-conjugated anti–IL-17A (N49-653) (both from BD Bioscience). Data were acquired using a BD FACS Aria III and analyzed with FlowJo software (BD Biosciences).

2.5. Bulk RNA- and TCR-sequencing

Total RNA was isolated from skin TLS-positive and -negative patients with pemphigus, TLS lesions before and after intralesional corticosteroid injection, and in vitro Treg-undepleted and Treg-depleted CXCL13-producing $CD4^+$ T cells using TRIzol (Invitrogen) reagent following the manufacturer's instructions. For bulk RNA-Seq, isolated total RNA was subjected to sequencing library production using the SureSelect RNA Direct kit (Agilent Technologies) for skin and the TruSeq Stranded mRNA Library Prep Kit (Illumina) for T cells according to the manufacturer's protocol. Briefly, the cDNA library was created with a thermal cycler and the exon regions captured using SureSelect XT Human All Exon V6+UTRs Kit (Agilent Technologies) for skin and the SMART-Seq v4 Ultra Low Input RNA kit (Takara Bio Inc.) for T cells. The captured libraries were sequenced by Novaseq (Illumina). For bulk TCR-Seq, isolated total RNA was subsequently amplified using human TCR chain primers for TCR libraries, which were sequenced by Miseq (Illumina).

2.6. Analysis of bulk RNA- and TCR-sequencing

To identify DEGs ($P < 0.001$, fold change >2 or <–2) in the bulk RNA-Seq data, the R package DEGseq was used. From the list of DEGs, an analysis of the GO categories was performed using the web-based tool EnrichR (https://maayanlab.cloud/Enrichr/). For gene

signature-specific analysis, the GSEA software was used. The reference gene sets of Th1, Th2, and Th17 cell and IL-2 pathway and gene sets of the Tfh cell related to human cancer TLSs[21]. The matrix visualization and analysis software Morpheus was used to draw a heatmap. In bulk TCR-Seq data, the proportion of top 10 clones of the TCRβ chains was calculated using the R package immunarch.

2.7. TCR sequencing of DSG3-specific T cells

Cryopreserved PBMCs from a patient with pemphigus were thawed and rested for 4 hours at 37°C. Cells were stimulated with 5 μg/mL recombinant human DSG3 protein (Cusabio) for 20 hours at 37°C in a 5% CO2 atmosphere. After stimulation, cells were incubated for 20 minutes at room temperature with a biotinylated anti-human-CXCR5 (RF8B2), followed by staining with BV421-conjugated streptavidin (both from BD Biosciences). Cells were washed and incubated with the following antibodies: BV510-conjugated anti-CD3 (UCHT1), PE-Cy7–conjugated anti-PD-1 (EH12.1), and APC-H7–conjugated anti-CD45RA (HI100) (all from BD Biosciences) and FITC-conjugated anti-CCR7 (G043H7), PerCP-Cy5.5–conjugated anti-CD4 (RPA-T4), PE-conjugated anti-CD25 (BC96), and APC-conjugated anti-CD134 (ACT35) (all from BioLegend). Dead cells were excluded using the LIVE/DEAD Fixable Red Dead Cell Stain Kit (Invitrogen). $CD134^{+}CD25^{+}$ (activation-induced marker) cTfh cells and non-cTfh memory $CD4^{+}$ T cells were sorted using a FACSAria III cell sorter (BD Biosciences) and cDNA synthesized using the SMARTer Human TCR α/β profiling kit (Takara Bio Inc.) according to the manufacturer's instructions. Purified TCR libraries were assessed and quantified using Bioanalyzer 2100 (Agilent Technologies). All libraries were pooled together for 1 run of Illumina MiSeq 2 × 300 bp sequencing.

2.8. Single-cell RNA and TCR sequencing

Skin tissue samples were obtained by 6 mm punch biopsy. After removal of subcutaneous fat, the tissues were chopped and digested with 50 mg/mL Collagenase 1A (Sigma-Aldrich) using a gentleMACS dissociator (Miltenyi Biotec) for 2 hours. After incubation, 1 mg/mL DNase I (Sigma-Aldrich) was added. Dead cells were excluded using the Live/Dead Fixable Near-IR Cell Stain kit (Invitrogen), and single cells were stained with BV421-conjugated anti-CD45 (HI30) and PE-conjugated anti-EpCAM (9C4) (both from BioLegend). Live $CD45^{+}EpCAM^{-}$ cells were sorted using a FACS Aria III cell sorter (BD Biosciences). scRNA-Seq and TCR-Seq libraries were generated using the Chromium single-cell 5' Library kit version 1.1, Chromium 5′ Gel Bead Kit version 1.1, and Chromium V(D)J Human T cell Enrichment Kit (10X Genomics) following

the manufacturer's instructions. Libraries were constructed and sequenced at a depth of 20,000 reads per cell for RNA or 5,000 reads per cell for TCR using the HiSeq 4000 platform (Illumina).

2.9. Single-cell RNA and TCR sequencing analysis

All downstream analyses were performed using Cell Ranger 7.0 and the R package Seurat (v4.0.4). Outlier gene detection rates (nFeautre_RNA <300 and >14,000) and high mitochondrial transcript load (>10%) were filtered from the analysis. The data were normalized using Seurat's logNormalize with a scale factor of 10,000. Data from individual samples were combined into a single expression matrix after scaling. Then, the cell cycle scores were set as variables to regress out. The Uniform Manifold Approximation and Projection (UMAP) algorithm was used to reduce and visualize dimensionality, followed by the construction of a clustering analysis. DEGs among clusters were detected by the Seurat function "FindAllMarkers." Select functional DEGs in each cluster were visualized via stacked violin plots. Volcano plots of DEGs ($P < 0.05$, log2 fold change >0.25 or <–0.25) were applied to show the genes with upregulated or downregulated expression using ggplot2. For TCR analysis, we selected the TCRβ repertoire. Unique clones were defined as single clones and nonunique clones as shared clones. Cell trajectory and pseudo-time analysis was performed using the Monocle 3 R package (v1.3.1). To examine whether particular GO terms were enriched in certain gene sets, we carried out GO enrichment analysis using EnrichR. GO categories with adjusted $P < 0.05$ were considered significant. Biocarta_IL2_pathway, wp_IL10_antiinflammatory_signaling_pathway, and tgf-beta signaling pathway were used as the IL-2, TGF-β, and IL-10 pathway gene set, respectively. The Seurat AddModuleScore was utilized to analyze the gene signature expression of TCR-mediated signaling and TRM cells. The TCR-mediated gene set was composed of *CALM1, CALM2, CALM3, CD247, CD3D, CD3E, CD3G, ELK1, FOS, FYN, GRB2, HRAS, JUN, LAT, LCK, MAP2K1, MAP2K4, MAP3K1, MAPK3, MAPK8, NFATC1, NFATC2, NFATC3, NFKB1, NFKBIA, PIK3CA, PIK3CG, PIK3R1, PLCG1, PPP3CA, PPP3CB, PPP3CC, PRKCA, PRKCB, PTPN7, RAC1, RAF1, RASA1, RELA, SHC1, SOS1, VAV1,* and *ZAP70*. The gene set of TRM cells was composed of *CXCL13, CXCR6, IL23R, ITGAE, PDCD1, CD69, FABP4, FABP5, ID2, ID3, NR4A1, IL10, IL2,* and *RUNX3*[22].

2.10. Multiplex immunohistochemistry staining and imaging

4 μm Formalin-fixed, paraffin-embedded tissue sections were used for imaging. Slides were heated for at least 1 hour in a dry oven at 60°C. The slides were dewaxed with Leica Bond Dewax solution (Leica Biosystems), and antigen retrieval was performed with Bond Epitope Retrieval 2 (Leica Biosystems) for 30 minutes. Primary antibody incubation was performed for 30 minutes

after blocking with 1× antibody diluent/block solution (Akoya Bioscience) followed by OPAL polymer HRP incubation for 10 minutes. Primary antibodies used included CD4 (EPR6855), CD20 (L26), FoxP3 (236A/E7), and PD-1 [EPR4877(2)] (all from abcam), CXCR5 (D6L3C, Cell Signaling Technology), and CXCL13 (R&D Systems). OPAL Polymer HRP anti-mouse were used for CD20, CXCR5, and FoxP3; anti-rabbit antibodies were used for CD4 and PD-1; and anti-goat were used for CXCL13. Visualization of the antigen was performed using tyramide signal amplification (Akoya Biosciences) for 10 minutes, and, to remove bound antibodies, slides antigen retrieval was performed with Bond Epitope Retrieval 1 (Leica Biosystems) for 20 minutes. The process from blocking to antigen retrieval was repeated for every antibody used. For counterstaining, nuclei were stained with DAPI (Thermo Fisher Scientific). Stained slides were imaged by using the Vectra Polaris Automated Quantitative Pathology Imaging System (Akoya Biosciences). Representative images for training were selected by the Penochart (Akoya Biosciences), and the negative and positive of each marker were trained using the inForm Image Analysis software (Akoya Bioscience) to validate the markers. Each single cell was segmented based on DAPI, and phenotyping was performed according to the expression and intensity of each marker. We designated $CXCL13^+CD4^+$ cells ($CXCL13^+CD4^+$ T cells), $CXCR5^+PD\text{-}1^+CD4^+$ cells (Tfh cells), $CXCR5^+FoxP3^+CD4^+$ cells (Tfr cells), $CXCR5^-FoxP3^+CD4^+$ cells ($CXCR5^-$ Tregs), and $CXCR5^+CD20^+$ cells ($CXCR5^+$ B cells). We selected 3 ROI with all existing $CXCL13^+CD4^+$ T cells, Tfr cells, Tfh cells, and naive B cells. To analysis the spatial cell-to-cell distance, the distance between the 2 nearest cells was calculated using the nearest neighbor analysis, and the distances of each target cell from the nearest $CXCL13^+CD4^+$ T cells were measured.

2.11. CODEX tissue staining and imaging

For multiplex tissue staining and acquisition, formalin-fixed, paraffin-embedded samples were mounted on no. 1.5 coverslips. Multiplex tissue staining and acquisition were performed by Enable Medicine in accordance with previously published methods[23]. Coverslips were imaged on an inverted fluorescence microscope (Keyence BX-810) using a Plan Apo 20x 0.75 NA objective (Nikon). The multiplex imaging cycles were performed on a CODEX (Akoya Biosciences). Raw CODEX data were processed by Enable Medicine using a cloud processing pipeline. Briefly, deconvolution and extended depth of field were computed for each Z-stack, and neighboring tiles and sequential cycles were computationally aligned and stitched together. Finally, background subtraction was performed by subtracting the linearly interpolated background signal between the first and final background acquisitions. Nuclear cell segmentation was performed using the Mesmer model from the DeepCell library[24]. Nuclear segmentation masks were stochastically dilated by flipping pixels with a probability equal to the fraction of positive neighboring pixels. This dilation was repeated for 9 cycles for all CODEX

data. Biomarker expression levels were computed from the mean pixel values within each segmentation mask for each cell. TLSs were manually annotated by drawing ROIs overlaid on the CODEX images using the Enable Medicine Portal. These ROIs were then used to filter cells for further downstream analysis. Downstream analysis was always restricted to cells filtered by ROI. Analysis was performed on a per-cell level, per-TLS level, or per-image level. Two different measures of spatial proximity were used in this study: (a) cells directly in contact and (b) nearest neighbors. To define cells directly in contact, we generated Voronoi tessellations from the centroids of the segmentation masks. Cells that shared an edge in the Delaunay dual of the Voronoi tessellation were defined as being in direct contact. Nearest neighbors were identified per cell type and defined using the Euclidean distance. Only cells within the same TLS were considered when calculating nearest neighbors. For certain biomarkers, manual gating was applied to define a threshold of positivity. Gating was performed on a per-image basis.

2.12. Computing cell density from imaging data

A moving-window density analysis was performed on the multiplexed tissue images to calculate the local density of target cells in the vicinity of individual $CXCL13^+$ or $CXCL13^-$ $CD4^+$ T cells with varying distances. Initially, after extracting cell position data from the ROIs, the subsequent the analyses were conducted on each ROI. A circle with a radius of 5 μm was initially positioned with its center on a selected cell. This circle was then expanded radially in increments of 1 μm, up to a maximum radius of 100 μm. The number of target cells present in each circle was counted, and the "edge-corrected" area of each circle was calculated by excluding the area of each circle that extended beyond the boundaries of the ROIs. To identify where the circle intersected with the ROI boundaries, the extract function from the terra package in R was used, customized for our specific application. Finally, target cell densities in "moving windows" were computed by sweeping ring-shaped regions called rings radially outward up to a maximum distance. Each ring was defined as the region between two circles with radii differing by a specified width. The area and cell count of each ring was then calculated by subtracting the area and cell counts of the inner circle from those of the outer circle, respectively, followed by the calculation of local densities of target cells.

2.13. Statistics

Data were statistically analyzed with Graphpad Prism Software version 9.2.0. Multiple comparisons were analyzed using 1-way ANOVA with Bonferroni's post hoc test. Statistical comparisons were analyzed by using 2-tailed Student's t test, 2-tailed paired t test, and Wilcoxon matched-pairs signed-rank test for 2 groups. Pearson's correlation analysis was used to measure

the strength of relationships between variables. *P* values of less than 0.05 were considered significant. All results are presented as mean ± SD. The significance of the difference between groups was analyzed as described in the figure legends.

Table 1. List of the abbreviations

Abbreviation	Definition
AIM	Activation-induced marker
CODEX	CO-Detection by indEXing
cTfh cell	circulating T follicular helper cell
DSG	Desmoglein
FDC	Follicular dendritic cell
GC	Germinal center
HEV	High endothelial venule
ILI	Intralesional corticosteroid injection
LTβ	Lymphotoxin β
PF	Pemphigus foliaceus
PNAd	Peripheral lymph node addressin
PNP	Paraneoplastic pemphigus
PV	Pemphigus vulgaris
ROI	Region of interest
SLO	Secondary lymphoid organ
TCR	T-cell receptor
Tfh cell	T follicular helper cell
Th cell	T helper cell
TLS	Tertiary lymphoid structure
Tm cell	Memory T cell
Treg	Regulatory T cell
Trm cell	Tissue-resident memory T cell

3. RESULTS

3.1. TLSs are commonly observed in the chronic skin lesions of patients with pemphigus.

We retrospectively reviewed H&E-stained slides of skin specimens from patients with pemphigus. Skin specimens with dense inflammatory cell infiltration into the dermis were selected from the slides. To analyze the phenotypes of immune cells infiltrating the dermis, we utilized immunohistochemistry to investigate expression of CD4, CD20, CD138, and peripheral lymph node addressin (PNAd). Tight clusters of $CD4^+$ T cells and $CD20^+$ B cells containing $PNAd^+$ high endothelial venules surrounded by $CD138^+$ plasma cells were observed in skin lesions from 6 patients with PV, 3 patients with PF, and 1 patient with PNP (**Figure 1A-D**). These TLSs include follicular dendritic cells (FDCs), $CD11c^+$ dendritic cells, $D2\text{-}40^+$ lymphatic vessels, and lymphotoxin β (**Figure 1E**). These findings indicate that TLSs can be present in pemphigus skin lesions with dense inflammatory cell infiltration into the dermis. Through examination of the clinical characteristics of the patients with TLSs, we found that the duration of skin lesions was at least 4 months (**Table 1**).

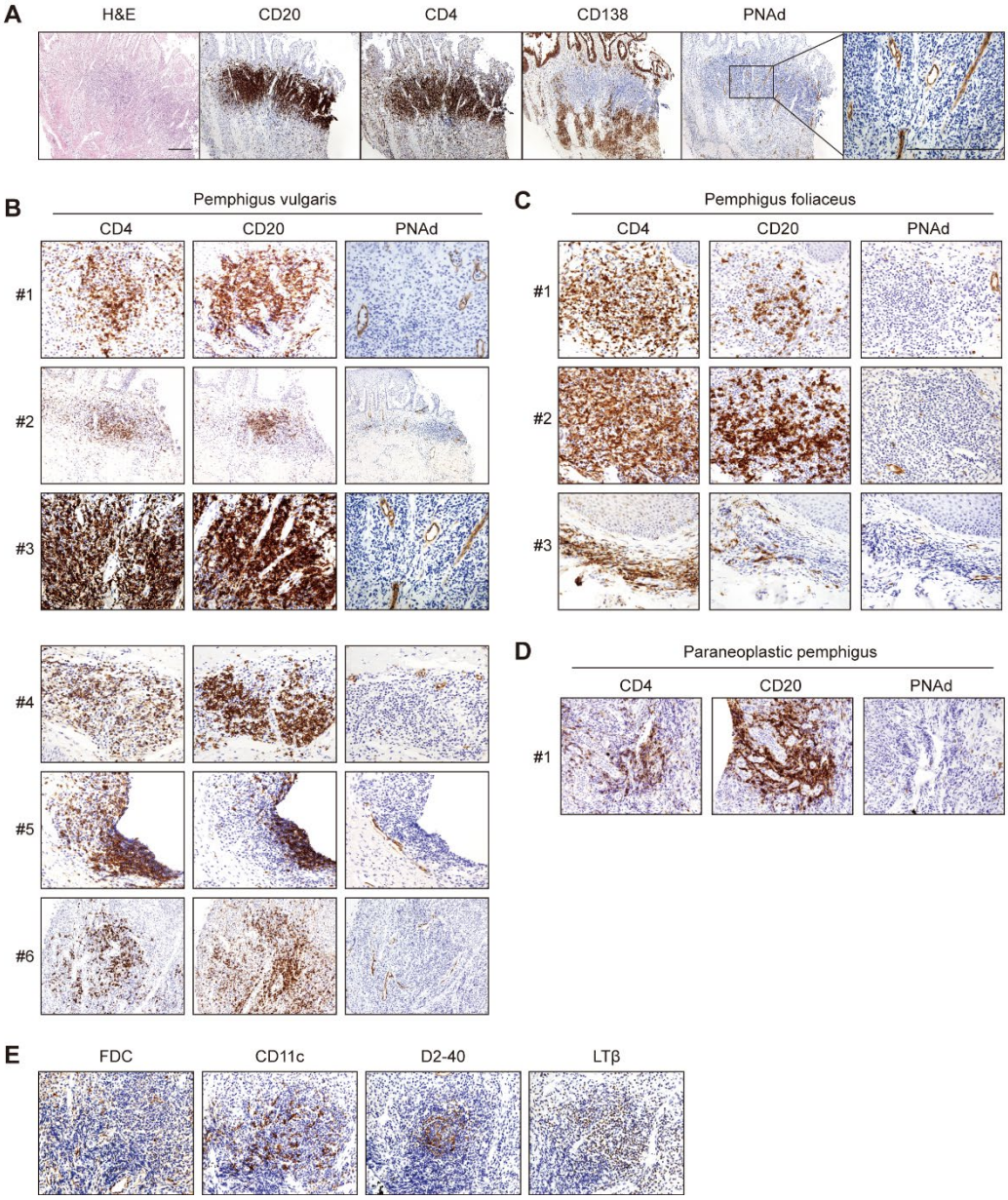

Figure 1. Histological features of skin tertiary lymphoid structures (TLSs) in patients with pemphigus from the retrospective study. (A) A representative skin biopsy sample from a patient with pemphigus vulgaris showing tertiary lymphoid structures (TLSs), stained with H&E and specific antibodies against CD20, CD4, CD138, and PNAd. (B-D) Immunohistochemical

staining for CD4, CD20, and PNAd was performed in patients with pemphigus vulgaris (n=6), pemphigus foliaceus (n=3), and paraneoplastic pemphigus (n=1). (E) Representative images of immunohistochemical staining for follicular dendritic cells (FDCs), CD11c, D2-40, and lymphotoxin β (LTβ). Scale bar: 100 μm.

Table 2. Characteristics of patients with pemphigus with skin TLSs in a retrospective review

	Age	Sex	Biopsy site	Duration of skin lesion (months)	Duration of diseases (years)	Treatment of methylprednisolone (mg/d)
PV1	48	Female	Lip	12	4	6
PV2	50	Female	Scalp	6	5	10
PV3	35	Female	Abdomen	14	4	2
PV4	60	Male	Scalp	4	18	8
PV5	77	Female	Cheek	12	2	8
PV6	65	Female	Lip	12	2	8
PF1	40	Female	Scalp	24	2	16
PF2	35	Male	Chest	6	0.5	16
PF3	35	Female	Back	10	1	6
PNP1	68	Male	Lip	4	4	0

PV, pemphigus vulgaris; PF, pemphigus foliaceus; PNP, paraneoplastic pemphigus.

3.2. Skin TLSs contribute to the pathogenicity in pemphigus.

To further analyze skin TLSs in pemphigus, we conducted a prospective study in which we enrolled patients with pemphigus who had chronic bullae persisting for more than 4 months. We obtained punch biopsies of the chronic lesions and carried out immunohistochemical studies for CD20, CD138, CD4, and PNAd to identify TLSs (**Figure 2A**). Of the 31 patients, 23 had skin samples positive for TLSs, whereas 8 were negative for TLSs **(Figure 2A** and **Table 2)**. More than half of the lesions with TLSs were located in the scalp (n = 13). The lesions with TLSs had a significantly longer duration than lesions without TLSs, and all skin TLSs were detected in blisters that persisted for at least 8 months (**Figure 2B**). When we investigated the antigen specificity in TLSs, we found that B cells and plasma cells specific for DSG3 and DSG1 were located at the edge of TLSs in samples from patients with PV and PF, respectively (**Figure 2C**). Taken together, these results confirm that TLSs with DSG-specific B cells and plasma cells are present in chronic blisters in patients with pemphigus.

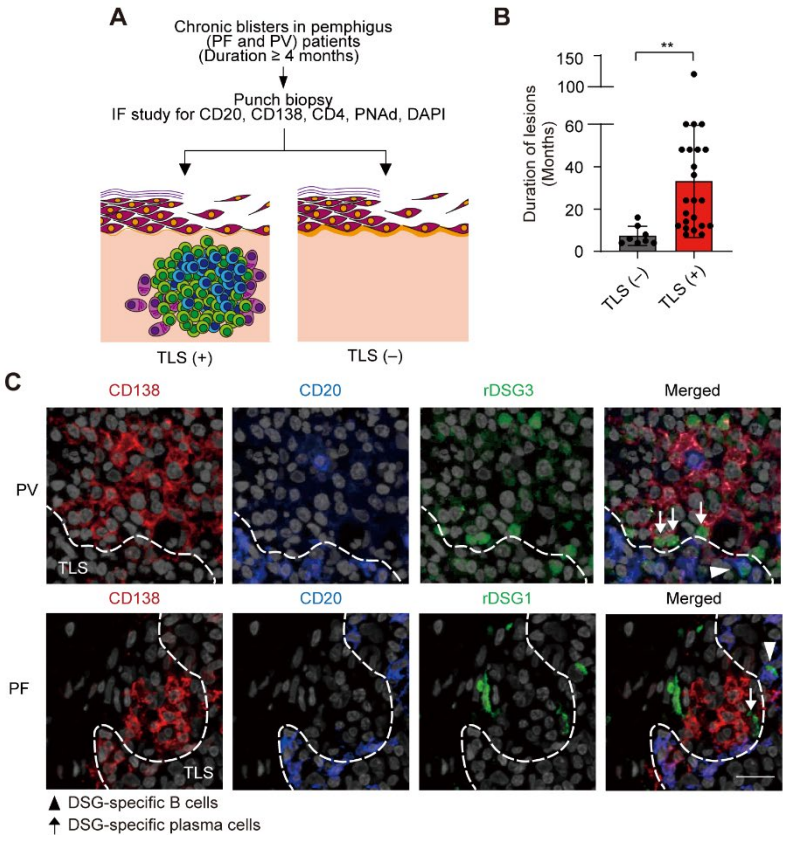

Figure 2. Skin tertiary lymphoid structures in chronic blisters of patients with pemphigus. (A) Schematic of the experiment. (B) Duration of skin blisters in TLS-negative (n = 8) and TLS-positive (n = 23) lesions. Means were compared between the two groups using Student's t tests. Data are shown as the mean ± SD. $^{**}P < 0.005$. (C) Representative immunofluorescence staining for DSG-specific B cells (triangles) and plasma cells (arrows). Tissues were stained with CD138 (red), CD20 (blue), rDSG1 or rDSG3 (green), and DAPI (light gray). Dotted lines indicate the margin of TLSs. Scale bar: 50 μm. PF, pemphigus foliaceus; PV, pemphigus vulgaris; rDSG1, recombinant desmoglein 1; rDSG3, recombinant desmoglein 3.

Table 3. List of patients with pemphigus in a prospective study

Patient No.	Sex	Disease	Biopsy site	TLS	CD4	CD20	CD138	PNAd
1	M	PV	back	+	+	+	+	+
2	F	PV	scalp	+	+	+	+	+
3	F	PF	scalp	+	+	+	+	+
4	F	PV	lip	+	+	+	+	+
5	F	PV	scalp	+	+	+	+	+
6	F	PF	scalp	+	+	+	+	+
7	M	PF	scalp	+	+	+	+	+
8	F	PV	scalp	+	+	+	+	+
9	F	PV	scalp	+	+	+	+	+
10	M	PV	back	+	+	+	+	+
11	M	PV	face	+	+	+	+	+
12	F	PV	scalp	+	+	+	+	+
13	M	PV	scalp	+	+	+	+	+
14	M	PF	scalp	+	+	+	+	+
15	F	PF	scalp	+	+	+	+	+
16	F	PV	scalp	+	+	+	+	+
17	M	PV	back	+	+	+	+	+
18	M	PV	back	+	+	+	+	+
19	F	PV	back	+	+	+	+	+
20	M	PF	back	+	+	+	+	+
21	M	PV	back	+	+	+	+	+
22	F	PF	chest	+	+	+	+	+
23	M	PF	scalp	+	+	+	+	+
24	F	PV	chest	–				
25	M	PF	leg	–				
26	M	PF	scalp	–				
27	F	PV	chest	–				
28	M	PF	neck	–				
29	F	PF	back	–				
30	F	PF	scalp	–				
31	M	PF	scalp	–				

M, male; F, female; PV, pemphigus vulgaris; PF, pemphigus foliaceus.

3.3. CXCL13 is upregulated in skin TLSs of pemphigus.

Next, we performed bulk RNA-Seq of pemphigus skin samples with TLSs (n = 5) and without TLSs (n = 5) and compared their gene signatures (**Figure 3A**). Consistent with the phenotypes, gene set enrichment analyses (GSEAs) showed that TLS-related gene signatures were upregulated in pemphigus skin lesions with TLSs compared with those without TLSs (**Figure 3B**). Gene ontology (GO) term analysis revealed that chemokine activity and chemokine receptor binding genes were upregulated in skin lesions with TLSs compared with those without TLSs (**Figure 3C**). We identified 14 differentially expressed genes (DEGs) belonging to chemokine and chemokine receptor gene sets (**Figure 3D**). Given that previous studies using conditional CXCL13-transgenic mice demonstrated that CXCL13 is sufficient to induce TLSs[25, 26], we focused on CXCL13 among the upregulated chemokines in skin lesions with TLSs.

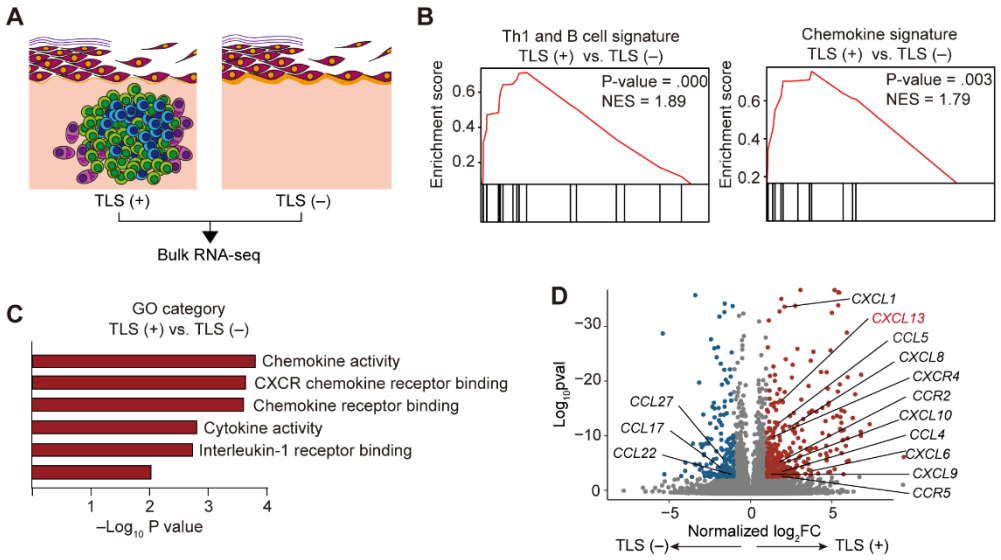

Figure 3. Expression of gene signatures in TLS-positive and -negative groups. (A) Schematic of the experiment for bulk RNA-Seq of tertiary lymphoid structure (TLS)–positive and TLS–negative samples (n = 5 each). (B) Gene set enrichment analysis (GSEA) of Th1 and B cell related signatures and chemokine gene signatures. (C) Gene ontology (GO) analysis and (D) volcano plot depicting upregulated (red dots) and downregulated DEGs (blue dots).

3.4. $CD4^+$ T cells are the major CXCL13-producding cells in skin TLSs.

In immunofluorescence studies, $CXCL13^+$ cells were mostly located in TLSs (**Figure 4A**). Next, we used various cell markers, including CD4, CD8, CD20, CD138, FDC, and HLA-DR, to identify CXCL13–producing cells (**Figure 4B**) and determined that the majority of $CXCL13^+$ cells were $CD4^+$ T cells (**Figure 4C** and **D**). In GSEA, Th1, Th17, and Tfh cell gene signatures were enriched in skin lesions with TLSs, but the Th2 cell gene signature was not (**Figure 5A**). Bulk TCRβ RNA-Seq was performed to evaluate the distribution of TCR clones in skin lesions with TLSs. The top 10 clones constituted more than 50% of the total TCRβ repertoire (**Figure 5B**). These data suggest that T cells, including $CXCL13^+CD4^+$ T cells, in chronic skins with TLSs share TCR clones and have the characteristics of Th1, Th17, or Tfh cells.

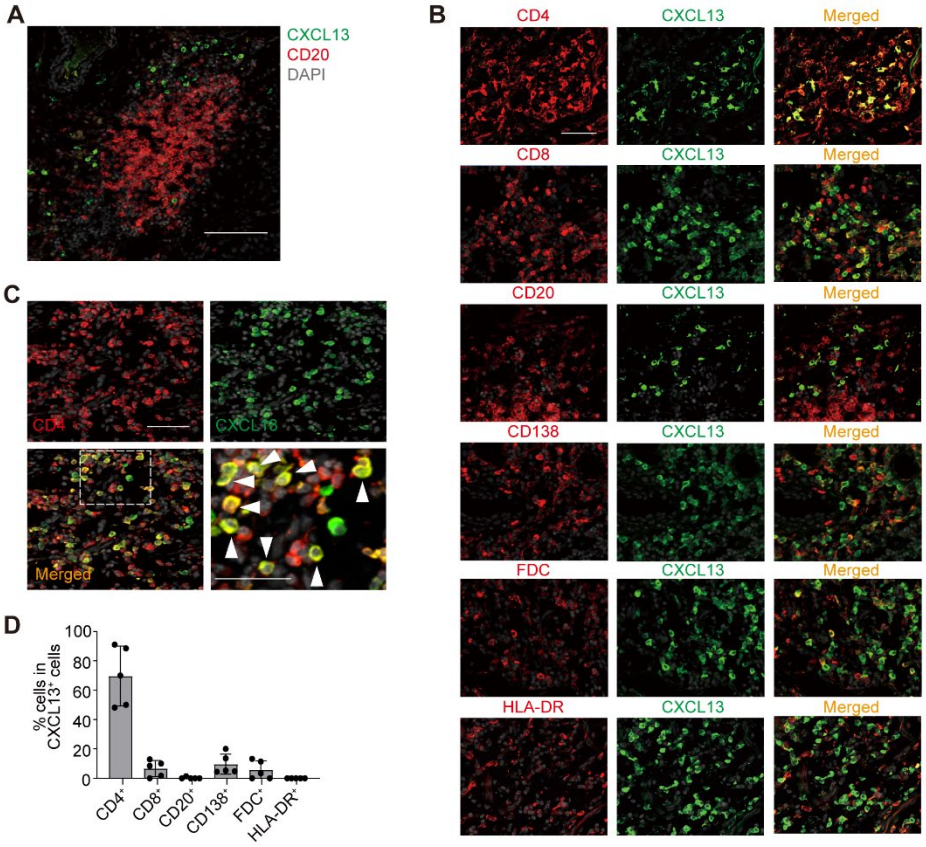

Figure 4. CD4$^+$ T cells are the major producer of CXCL13 in skin TLSs in pemphigus. (A) Representative immunofluorescence staining for CXCL13 (green) and CD20 (red) in skin TLSs from a patient with pemphigus. Nuclei were stained with DAPI (light gray). Scale bar: 100 μm. (B) Immunofluorescence staining for CXCL13 (green) with CD4, CD8, CD20, CD138, FDC, or HLA-DR (all red). Nuclei were stained with DAPI (light gray). Scale bar: 100 μm. (C) Representative immunofluorescence staining showing coexpression of CD4 (red) and CXCL13 (green) in skin TLSs. White arrowheads indicate CXCL13$^+$CD4$^+$ cells. Nuclei were stained with DAPI (light gray). Scale bar: 50 μm. (D) Percentage of CD4$^+$, CD8$^+$, CD20$^+$, CD138$^+$, FDC$^+$, and HLA-DR$^+$ cells in CXCL13$^+$ cells from immunofluorescence images (n = 5). Data are shown as mean ± SD.

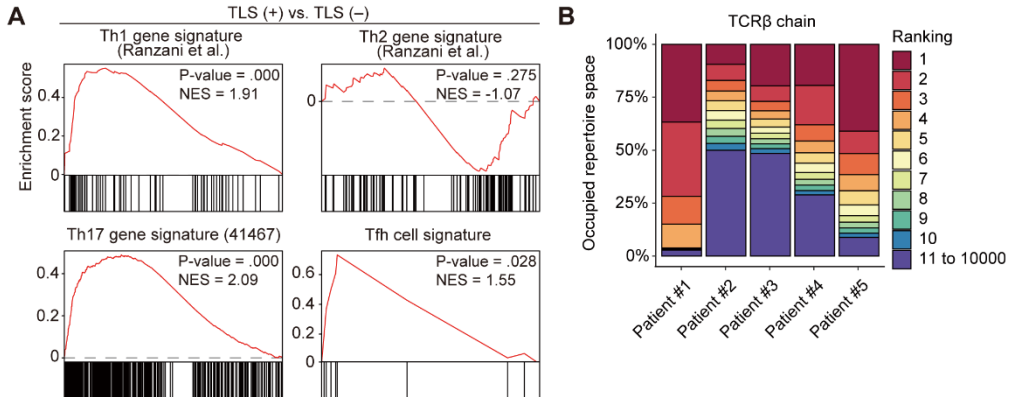

Figure 5. Analysis of Th1, Th2, Th17, and Tfh cell gene signatures and TCR clone distribution in skin lesions with TLSs. (A) Gene set enrichment analysis (GSEA) of Th1, Th2, Th17, and Tfh cell gene signatures comparing the transcriptome of TLS-positive versus TLS-negative samples. (B) Percentage of the top 10 most frequent TCRβ chain clones from bulk TCR-Seq in skin TLSs from 5 patients (no. #1–5).

3.5. CXCL13^{+}CD4^{+} T cells are clonally expanded and contain DSG-specific T cells in skin TLSs.

Next, we performed single-cell RNA-Seq (scRNA-Seq) combined with single-cell TCR sequencing (scTCR-Seq) in samples from 4 chronic skin lesions that had lasted at least 1 year. Live CD45^{+} cells were sorted from most parts of the skin, and immunofluorescence studies confirmed the presence of skin TLSs using the remaining part of the skin (**Figure 6A** and **B**). After quality control and doublet exclusion (**Figure 6C**), we obtained a total of 2,770 cells with 17 different clusters from all patient samples (**Figure 6D**). To analyze T cells, we focused on 2,141 cells that were positive for TCRβ in 10 clusters (**Figure 6E**).

We observed 6 clusters of TCRβ^{+} T cells in skin lesions with TLSs (**Figure 7A**). We further identified 3 clusters of CD4^{+} T cells expressing *CCR7* and *SELL*, corresponding to naive or circulating memory T cells, and 2 clusters of activated T cells expressing *TNFRSF18* encoding *GITR* (**Figure 7B).** Next, we evaluated TCR sharing and diversity in each cluster. Two activated CD4^{+} T cell clusters (clusters 1 and 5) shared their TCRs (**Figure 7C** and **D**), with cluster 5 being more clonal than cluster 1 (**Figure 7E**). Monocle 3 analysis showed that these 2 activated CD4^{+} T cell clusters are differentiated from 1 branch (**Figure 7F**). To determine whether these clusters have DSG-specific autoreactive T cells, we identified the TCR repertoire in DSG3-reactive, activation-induced marker^{+} CD4^{+} T cells in PBMCs from 1 patient with PV and matched TCRβ clones from the result to the TCR repertoire from scTCR-Seq from the same patient. We found that DSG-specific non-circulating Tfh (non-cTfh) memory CD4^{+} T cells, but not DSG-specific cTfh cells, were located in clusters 1 and 5 (**Figure 7G**). These data suggest that these 2 activated CD4^{+} T cell populations are clonally expanded.

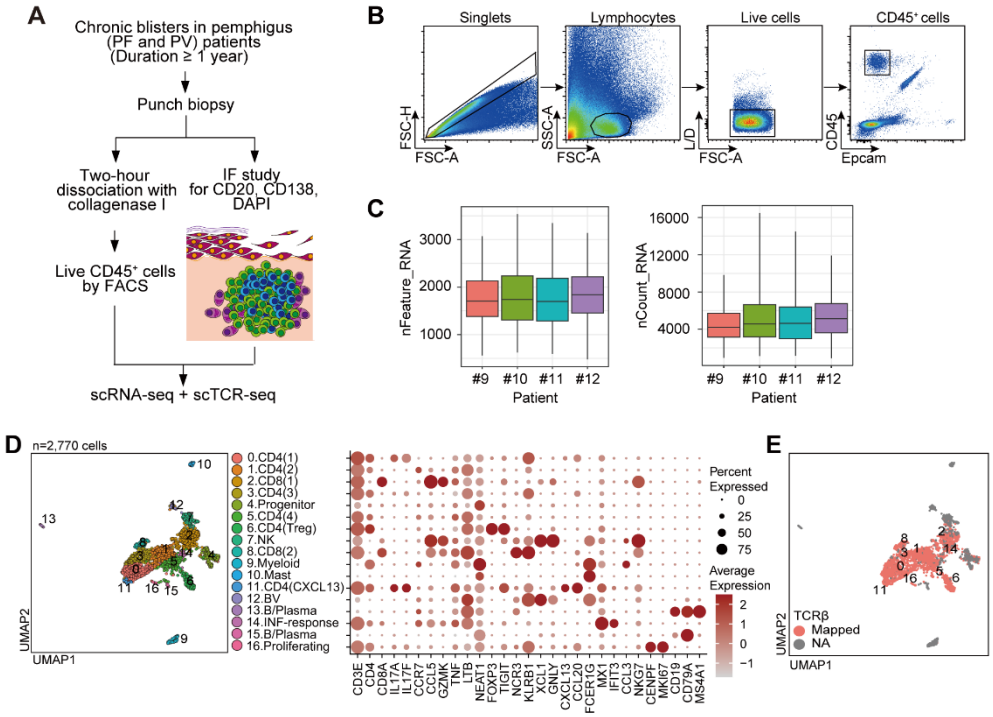

Figure 6. Single-cell RNA-Seq (scRNA-Seq) and single-cell TCR-seq (scTCR-Seq) of chronic TLS skin lesions. (A) Schematic of scRNA-Seq and scTCR-Seq for skin lesions with tertiary lymphoid structures (TLSs) in patients with pemphigus (n = 4). (B) Gating strategy for flow cytometric analysis of live CD45^{+} cells in skin TLSs. L/D, Live/Dead. (C) Distribution of all expressed gene numbers and expressed genes in each sample. (D and E) UMAP visualization of 2,770 cells with 17 clusters in all patients (D) and TCRβ^{+} cells with 10 clusters (E).

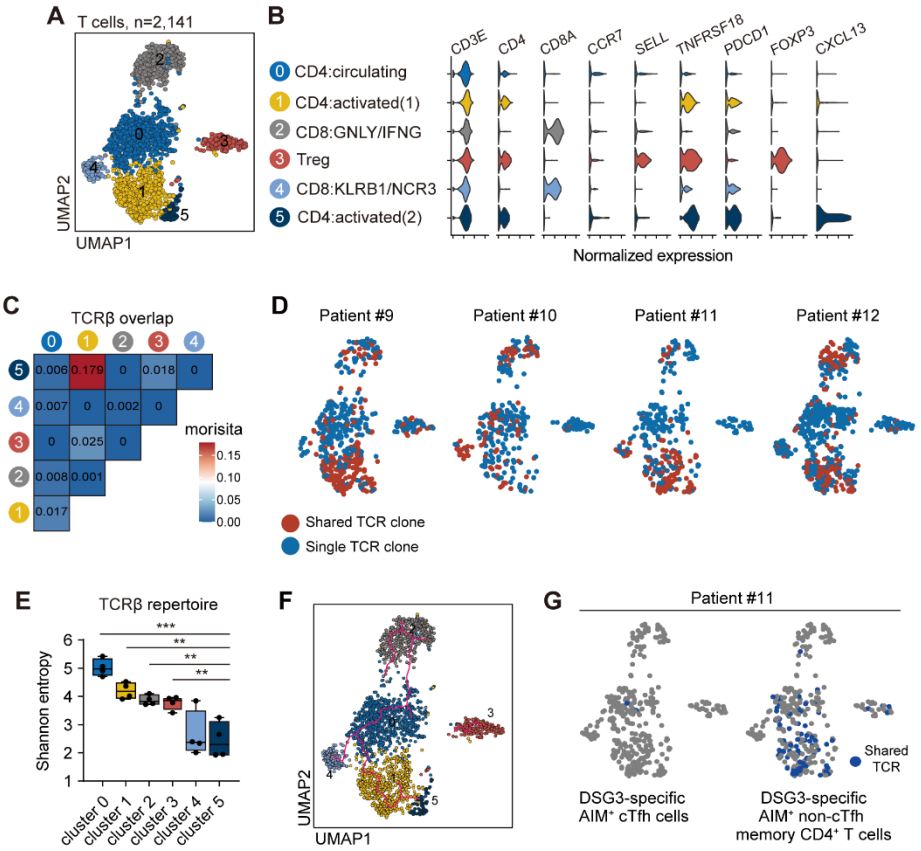

Figure 7. CXCL13$^+$CD4$^+$ T cells are clonally expanded and contain DSG-specific T cells in skin TLSs. (A) UMAP visualization of 2,141 TCRβ$^+$ T cells. (B) Violin plot showing the expression of the indicated marker genes in T cell subsets analyzed by scRNA-Seq. CD4, CD4$^+$ T cells; CD8, CD8$^+$ T cells. (C) Heatmap of the Morisita-Horn index quantifying overlapping TCRs among clusters. (D) Visualization of TCR clonality in each patient. Red dots indicate shared TCR clones and blue dots indicates single TCR clones. (E) Shannon entropy calculation of the diversity of the TCR repertoire in each cluster. One-way ANOVA and Student's t tests were used to compare means between two groups. $^{**}P < 0.005$; $^{***}P < 0.0001$. Data are shown as the mean ± SD. (F) Trajectory analysis of each cluster. (G) UMAP visualization of shared TCRs between T cells in skin TLSs and DSG3-specific, activation-induced marker (AIM)$^+$ Tfh and non-Tfh memory CD4$^+$ T cells in PBMCs from a patient with pemphigus vulgaris.

3.6. CXCL13^{+}CD4^{+} T cells with Th1-like features are activated in skin TLSs.

To characterize CXCL13^{+}CD4^{+} T cells, we compared the gene expression between two activated CD4^{+} T cell populations (**Figure 8A**). Analysis of DEGs revealed higher expression of *CXCL13* in cluster 5. We also found that cluster 5 had upregulated expression of *IFNG*, *BHLHE40*, and cytotoxicity-associated genes (*GZMB* and *NKG7*). Additionally, genes related to T cell activation (*TNFRSF9*, and *TNFRSF18*) and exhaustion (*LAG3* and *TIGIT*) were upregulated in cluster 5 (**Figure 8A**). Furthermore, the gene signature of tissue-resident memory T (Trm) cells was most highly expressed in cluster 5 (**Figure 8B**). To confirm that these features are consistent with those of CXCL13^{+}CD4^{+} T cells, we divided them into *CXCL13*-expressing and *CXCL13*-nonexpressing groups in clusters 1 and 5 (**Figure 8C** and **D**). We found that CXCL13^{+} cells expressed genes similar to those of cluster 5 (**Figure 8E**). Moreover, we observed that 38.1% of *CXCL13*-expressing cells also expressed the *IFNG* gene (**Figure 8D**). As CXCL13^{+}CD4^{+} T cells exhibited both an activated and exhausted phenotype, we further analyzed which phenotype was associated with the expression of *CXCL13*. We observed upregulation of glycolysis-associated genes (*TPI1* and *PGAM1*) in cluster 5 (**Figure 8F**). In cells from clusters 1 and 5, the expression of *TNFRSF18, TPI1*, and *PGAM1* positively correlated with the expression of *CXCL13* but not the expression of *LAG3* and *TIGIT* (**Figure 8G**).

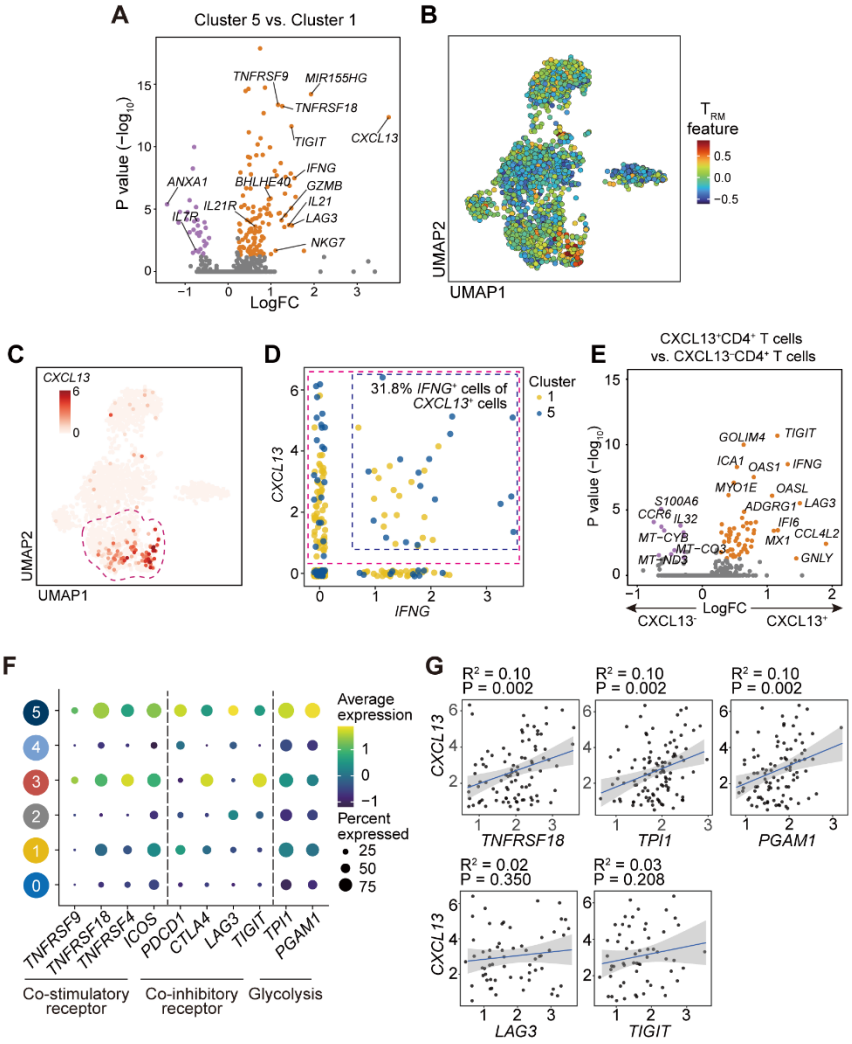

Figure 8. CXCL13^{+}CD4^{+} T cells are activated with Th1-like features. (A) Volcano plot showing upregulated (orange dots) and downregulated (purple dots) in cluster 5 DEGs compared with cluster 1. (B) UMAP visualization showing gene signature of tissue-resident memory T (Trm) cells. (C) *CXCL13* expression shown in UMAP. The red dotted line indicates clusters 1 and 5. (D) Expression of *CXCL13* and *IFNG* in cluster 1 and 5. The red dotted line indicates CXCL13^{+} cells and the blue dotted line indicates *IFNG*-expressing cells of CXCL13^{+} cells. (E) Volcano plot showing DEGs up-regulated (orange dots) and down-regulated (purple dots) in CXCL13^{+}CD4^{+} T cells compared to CXCL13^{-}CD4^{+} T cells. (F) Dot plot showing expression of genes in the categories of costimulatory or coinhibitory receptors and glycolysis in each cluster.

(G) Linear regression analyses of the expression of *CXCL13* and the correlation with expression of *TNFRSF18, TPI1, PGAM1, LAG3*, and *TIGIT* in clusters 1 and 5. Pearson's correlation analysis was used to measure the strength of relationships between variables.

3.7. $CXCL13^{+}CD4^{+}$ T cells downregulate TCR-mediated signaling when highly expressing *CXCL13*.

GO term analysis of cluster 5 compared with cluster 1 revealed that genes associated with cell cycle and glycolysis were upregulated, whereas genes associated with TCR binding were downregulated (**Figure 9A**). TCR-mediated genes were particularly downregulated in cluster 5, and *LCK* tended to negatively correlate with expression of *CXCL13* (**Figure 9B** and **C**). Taken together, these data suggest that clonally expanded $CXCL13^{+}CD4^{+}$ T cells have features of Th1-like cells but downregulate genes associated with TCR-mediated signaling when the expression of *CXCL13* was highly expressed.

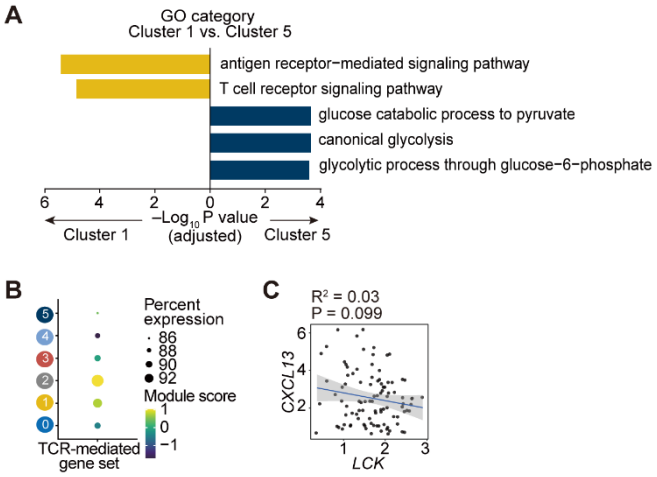

Figure 9. CXCL13^{+}CD4^{+} T cells have a feature of downregulation in TCR-mediated genes. (A) Gene ontology analysis in cluster 5 compared with cluster 1. (B) Dot plot depicting the TCR-mediated gene set in each cluster. (C) Linear regression analysis of the correlation between *CXCL13* and *LCK* in clusters 1 and 5. Pearson's correlation analysis was used to measure the strength of relationships between variables.

3.8. CXCL13^{+}CD4^{+} T cells are spatially adjacent to Tregs.

TCR stimulation induces expression of CXCL13 in CD4^{+} T cells in vitro[27]. In contrast, we observed downregulation of genes associated with TCR signaling in CXCL13^{+}CD4^{+} T cells within skin TLSs. To understand this phenomenon, we investigated the microenvironment and spatial organization of CXCL13^{+}CD4^{+} T cells. In order to identify the cells that are spatially associated with CXCL13^{+}CD4^{+} T cells, we employed a highly multiplex imaging technique, CO-Detection by indEXing (CODEX), with 41 protein markers to examine cell populations that interact with CXCL13^{+}CD4^{+} T cells (**Figure 10** and **Table 3**). We used formalin-fixed, paraffin-embedded tissues of chronic blisters from 36 TLSs in 10 patients with pemphigus to perform single-cell segmentation, assign cell type annotation by manual gating, visualize cell type using Voronoi diagrams to simplify the images, and analyze the data after selecting TLSs as ROIs (**Figure 11A** and **B**).

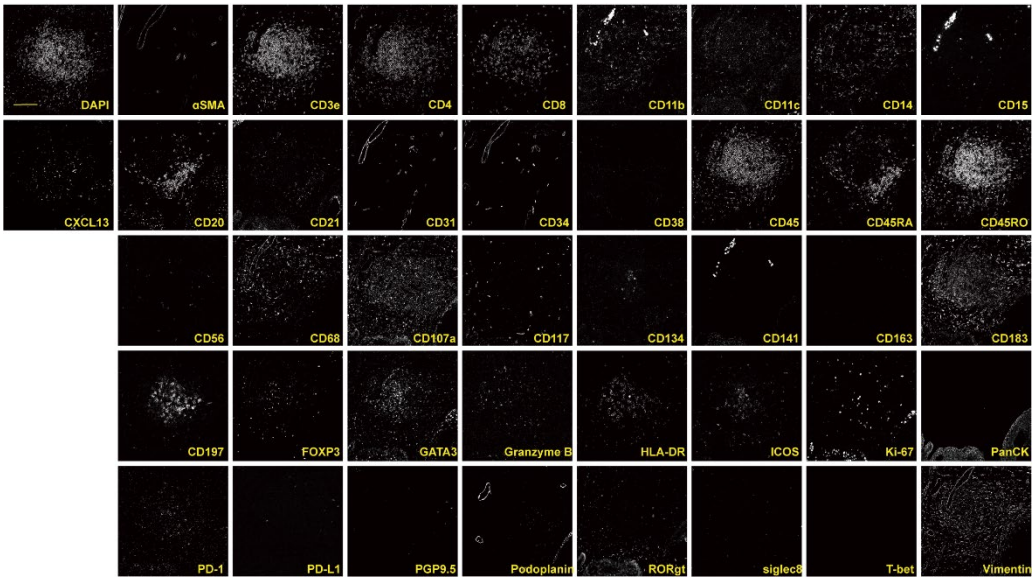

Figure 10. Validation of the antibody panel in spatial proteomics. Representative images of a skin TLS stained with 41 different antibodies by CODEX. Scale bar = 100 μm.

Table 4. List of antibodies for CODEX

No.	Antigen	Clone	Fluorophore
1	aSMA	EPR5368	Cy5
2	CD107a	H4A3	Cy5
3	CD117	YR145	Cy5
4	CD11b	EP1345Y	Atto 550
5	CD11c	118/A5	Cy5
6	CD134	Ber-ACT35	Atto 550
7	CD14	EPR3653	AF 750
8	CD141	E7Y9P	AF 750
9	CD15	HI98	AF 750
10	CD163	EPR19518	Atto 550
11	CD183	G025H7	Cy5
12	CD197	EPR23192-57	Cy5
13	CD20	L26	AF 750
14	CD21	EP3093	Atto 550
15	CD31	EP3095	AF 750
16	CD34	QBEND/10	AF 750
17	CD38	EPR4106	Atto 550
18	CD3e	EP449E	Cy5
19	CD4	EPR6855	Cy5
20	CD45	D9M8I	Cy5
21	CD45RA	HI100	AF 750
22	CD45RO	UCHL1	Atto 550
23	CD56	MRQ42	Atto 550
24	CD68	KP1	Cy5
25	CD8	C8/144B	Atto 550
26	CXCL13	AF801	Atto 550
27	FoxP3	259D/C7	AF 750
28	GATA3	L50-823	Atto 550
29	GranzymeB	D6E9W	Cy5
30	HLA-DR	EPR3692	Cy5
31	ICOS	D1K2T	Atto 550
32	Ki67	B56	Atto 550
33	PanCK	AE-1/AE-3	AF 750
34	PD1	D4W2J	AF 750
35	PDL1	E1L3N	AF 750
36	PGP9.5	EPR4118	AF 750
37	Podoplanin	NC-08	Atto 550
38	RORgammaT	6F3.1	AF 750
39	Siglec8	polyclonal	Atto 550
40	Tbet	EPR9302	AF 750
41	Vimentin	D21H3	AF 750

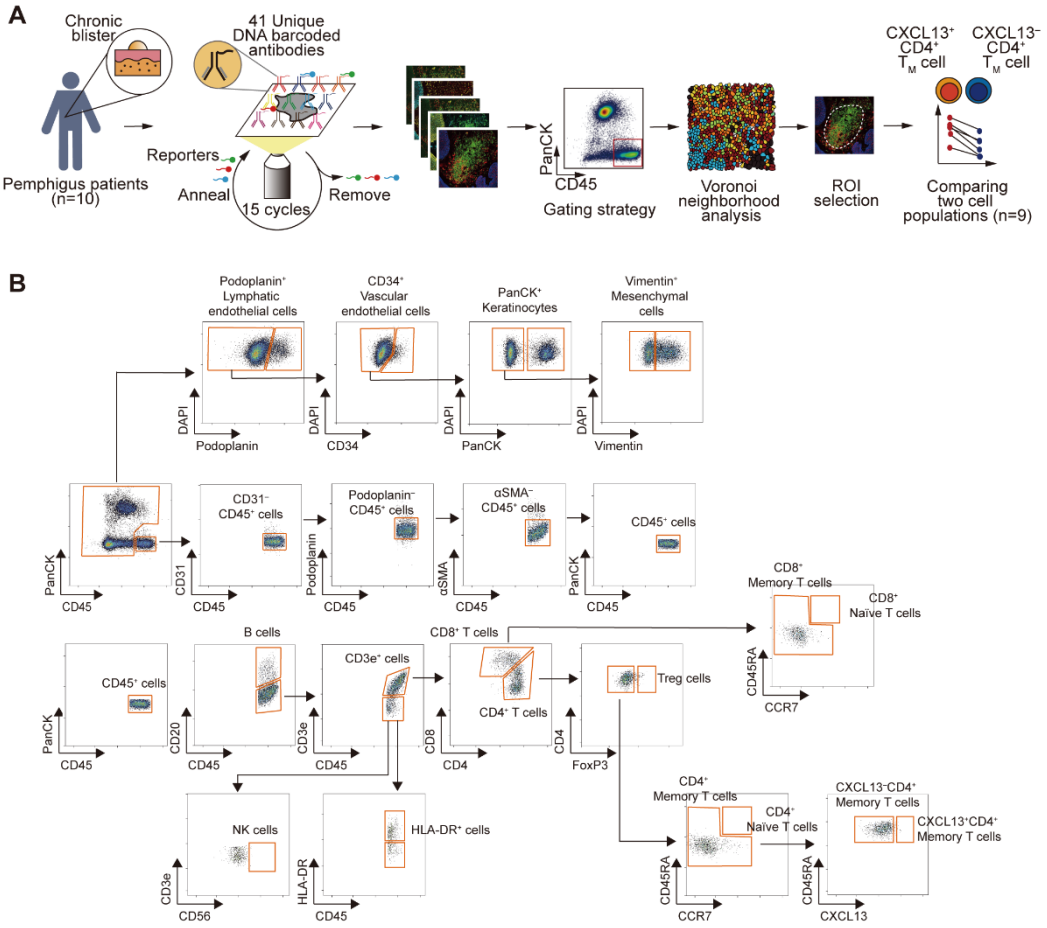

Figure 11. Spatial analysis of CXCL13^{+}CD4^{+} T cells. (A) Workflow for CODEX imaging and analysis of skin tertiary lymphoid structures (TLSs) in patients with pemphigus (n=9). (B) Spatial proteomics gating strategy for cell type annotation.

We mainly investigated the immune cell types among T cells, including $CXCL13^+$ and $CXCL13^-$ cells in $CD4^+$ memory T (Tm) cells, $CD8^+$ T cells, and $FoxP3^+CD4^+$ Tregs. We also examined $CD20^+$ B cells and HLA-DR^+ cells (**Figure 12A**). After excluding 1 tissue that had fewer than 10 $CXCL13^+CD4^+$ Tm cells in an image, we compared immunophenotypes and neighboring cell frequencies between $CXCL13^+CD4^+$ Tm cells and $CXCL13^-CD4^+$ Tm cells in 32 TLSs from the 9 images. $CXCL13^+CD4^+$ Tm cells had higher expression of PD-1 than $CXCL13^-CD4^+$ Tm cells (**Figure 12B**). In TLSs, we first computed the density of immune cell types (Tregs, $CD8^+$ T cells, B cells, and HLA-DR^+ cells) surrounding $CXCL13^+$ and $CXCL13^-CD4^+$ Tm cells. Contrary to the data observed for $CD8^+$ T cells, B cells, and HLA-DR^+ cells, we observed a significantly higher density of Tregs located 16.5 μm away from the center of $CXCL13^+CD4^+$ Tm cells compared with their density around $CXCL13^-CD4^+$ Tm cells (**Figure 12C**). We further examined the frequencies of these immune cell types directly adjacent to $CXCL13^+$ and $CXCL13^-CD4^+$ Tm cells. We found that the frequencies of Tregs adjacent to $CXCL13^+CD4^+$ Tm cells was significantly increased compared with that of $CXCL13^-CD4^+$ Tm cells (**Figure 12D** and **E**). When analyzing the expression markers in neighboring cell populations, no difference was found between all neighboring cells, including Tregs, adjacent to $CXCL13^+$ and $CXCL13^-CD4^+$ Tm cells (**Figure 12F** and **G**).

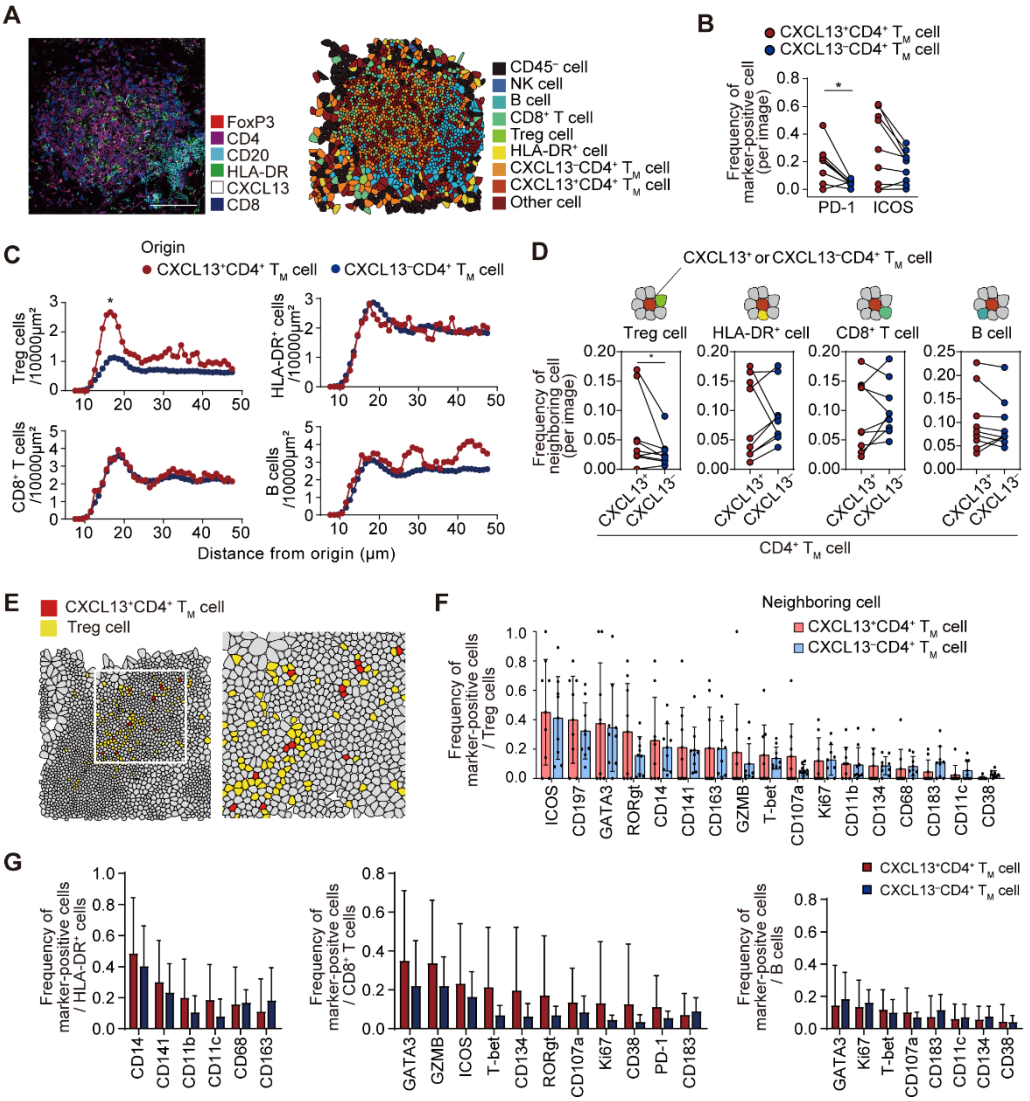

Figure 12. Tregs are adjacent to CXCL13$^+$CD4$^+$ T cells. (A) Six representative markers (left) for FoxP3 (red), CD4 (magenta), CD20 (cyan), HLA-DR (green), CXCL13 (white), and CD8 (blue) and a representative Voronoi diagram (right) of the TLSs after cell type mapping. (B) Frequency of PD-1$^+$ and ICOS$^+$ cells in CXCL13$^+$ versus CXCL13$^-$CD4$^+$ Tm cells. Paired t tests were used to compare values for 2-variable plots. *$P < 0.05$. (C) Densities of Tregs, HLA-DR$^+$ cells, CD8$^+$ T cells, and B cells based on their distance from the center of CXCL13$^+$ versus CXCL13$^-$CD4$^+$ Tm cells. Wilcoxon matched-pairs signed-rank test. *$P < 0.05$. (D) Frequencies

of Tregs, HLA-DR$^+$ cells, CD8$^+$ T cells, and B cells adjacent to CXCL13$^+$ versus CXCL13$^-$CD4$^+$ Tm cells in TLSs. Paired t tests were used to compare values for 2-variable plots. *$P < 0.05$. (E) Representative figures highlighting CXCL13$^+$CD4$^+$ Tm cells (red) and Tregs (yellow) in the Voronoi diagram. (F) Frequencies of marker-positive cells in Tregs adjacent to CXCL13$^+$ versus CXCL13$^-$CD4$^+$ Tm cells. Data are shown as the mean ± SD. (G) Frequencies of marker-positive cells in HLA-DR$^+$ cells, CD8$^+$ T cells, and B cells adjacent to CXCL13$^+$ versus CXCL13$^-$CD4$^+$ Tm cells.

Next, we utilized multiplex immunohistochemistry to analyze the spatial relationship between $CXCL13^+CD4^+$ T cells and $CXCR5^+$ cells using specific markers for CD4, CXCL13, CD20, FoxP3, CXCR5, and PD-1 (**Figure 13A**). Interestingly, we observed that $CXCR5^+$ B cells and $CXCR5^+PD\text{-}1^+$ Tfh cells tend to be in proximity to $CXCL13^+CD4^+$ T cells, rather than being directly adjacent to them (**Figure 13B**). Furthermore, with regard to Tregs adjacent to $CXCL13^+CD4^+$ T cells, we observed a higher frequency of $CXCR5^-$ Tregs compared with $CXCR5^+$ T follicular regulatory (Tfr) cells (**Figure 13C**). Taken together, these findings indicated that Tregs are spatially adjacent to $CXCL13^+CD4^+$ T cells within the skin TLSs.

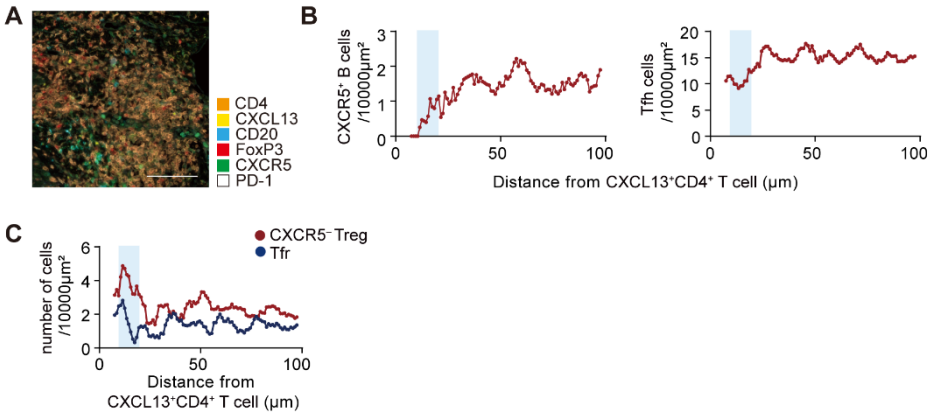

Figure 13. Analysis of multiplex immunohistochemistry (mIHC) for various CXCR5$^+$ cells adjacent to CXCL13$^+$CD4$^+$ T cells. (A) A representative image of mIHC by Vectra Polaris. Scale bar = 100 μm. (B and C) Densities of Tfh cells, CXCR5$^+$ B cells (B), CXCR5$^-$ Tregs, and Tfr cells (C) based on their distance from the center of CXCL13$^+$CD4$^+$ T cells. Number of ROI = 3. The highlighted bule regions are the location of 10-20 μm away from the center of CXCL13$^+$CD4$^+$ T cells.

3.9. Tregs increase the production of CXCL13 in $CD4^+$ T cells.

To address whether and how Tregs regulate CXCL13 expression on $CD4^+$ T cells, we used in vitro differentiation of $CXCL13^+CD4^+$ T cells (**Figure 14A**). Based on our scRNA-Seq data showing upregulation of *TNFRSF9* and *TNFRSF18* in $CXCL13^+CD4^+$ T cells, we used 4-1BB and GITR as activation markers in our in vitro studies. Our results showed that approximately 30% of $CXCL13^+CD4^+$ T cells were $4\text{-}1BB^+$ cells, while almost 100% of $CXCL13^+CD4^+$ T cells were $GITR^+$ cells (data not shown). Therefore, we selected GITR as a feasible marker to specifically evaluate the frequency of $CXCL13^+CD4^+$ T cells in activated T cells. Although the frequencies of IFN-γ^+, TNF-α^+, and IL-$17A^+$ cells did not differ between the conditions of Treg presence and absence (**Figure 14E**), we observed a reduction in the frequencies of $CXCL13^+$ cells in both $CD4^+$ T cells and $GITR^+CD4^+$ T cells in the absence of Tregs (**Figure 14B** and **C**). Tregs did not secrete CXCL13 in this condition (**Figure 14D**).

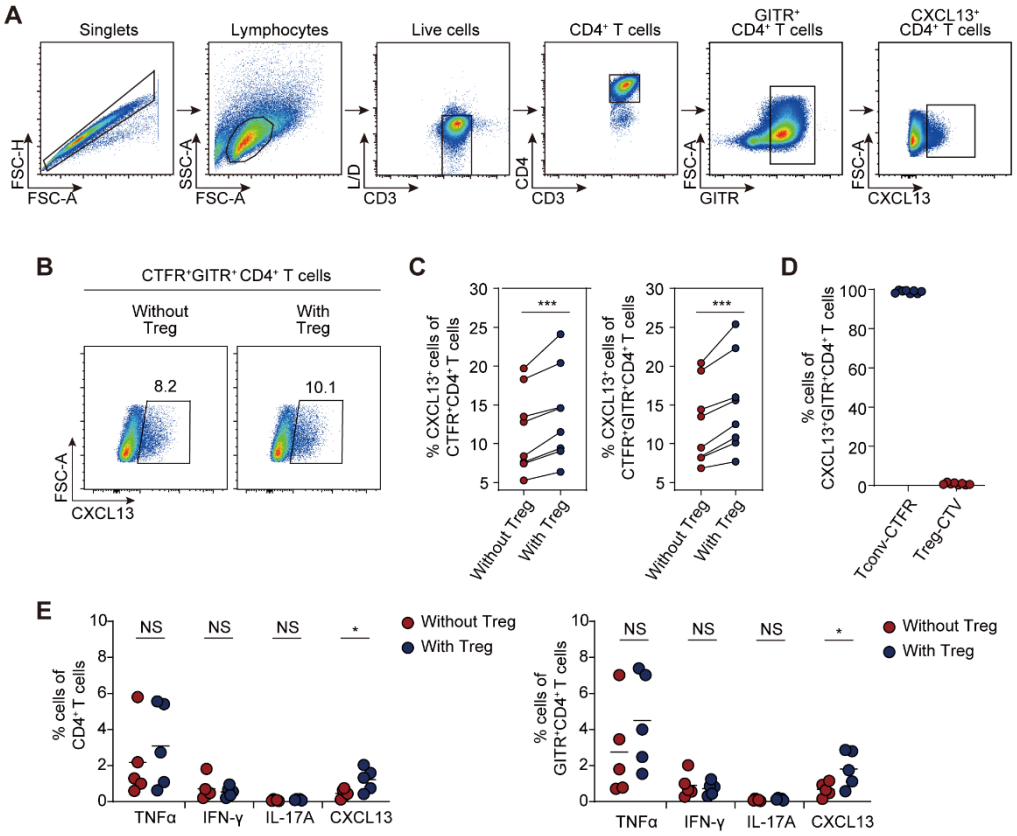

Figure 14. The production of CXCL13 in CD4$^+$ T cells is increased by Tregs. (A) Gating strategy for flow cytometric analysis of CXCL13$^+$CD4$^+$ T cells in vitro. L/D, Live/Dead. (B-D) CXCL13$^+$CD4$^+$ T cells were differentiated in with and without Treg conditions in vitro. CD25$^+$CD127^{lo}CD4$^+$ Tregs were stained with Cell Trace Violet (CTV) and Conventional CD4$^+$ T cells were stained with Cell Trace Far Red (CTFR). (B) Representative plots and (C) graph of the relative frequencies of CXCL13$^+$ cells in CTFR$^+$CD4$^+$ and CTFR$^+$GITR$^+$CD4$^+$ T cells (n = 8). (D) Frequencies of CTFR$^+$ conventional T cells and CTV$^+$ Tregs in CXCL13$^+$GITR$^+$CD4$^+$ T cells. (E) Graph showing the frequencies of IFN-γ$^+$, TNF-α$^+$, and IL-17A$^+$ cells in the conditions of Treg presence and absence. Paired t tests were used to compare values for 2-variable plots. NS, not significant; *$P < 0.05$; ***$P < 0.0001$.

To identify the factors regulating CXCL13 production, we compared bulk RNA-Seq profiles of $CD4^+$ T cells after the differentiation of $CXCL13^+$ cells in the presence or absence of Tregs. When evaluating GO term analysis and GESA, we found a significant decreased in gene expression involved in the IL-2–signaling pathway when differentiation occurred in the presence of Tregs (**Figure 15A-C**). In cluster 5 of the scRNA-Seq data, genes associated with the IL-2 pathway were downregulated and genes associated with TGF-β were particularly upregulated (**Figure 15D**). Next, we found that TGF-β and anti–IL-2–blocking antibodies synergistically increased CXCL13 expression in $CD4^+$ T cells (**Figure 15E**). In vitro coculture of induced Tregs (iTregs) and differentiated $CXCL13^+CD4^+$ T cells (**Figure 16A** and **B**) resulted in increased CXCL13 production by $CD4^+$ T cells, which was normalized when adding recombinant IL-2 protein and TGF-β–blocking antibody (**Figure 16C** and **D**). Taken together, these data suggest that Tregs increase CXCL13 expression in $CD4^+$ T cells through IL-2 deprivation and TGF-β stimulation.

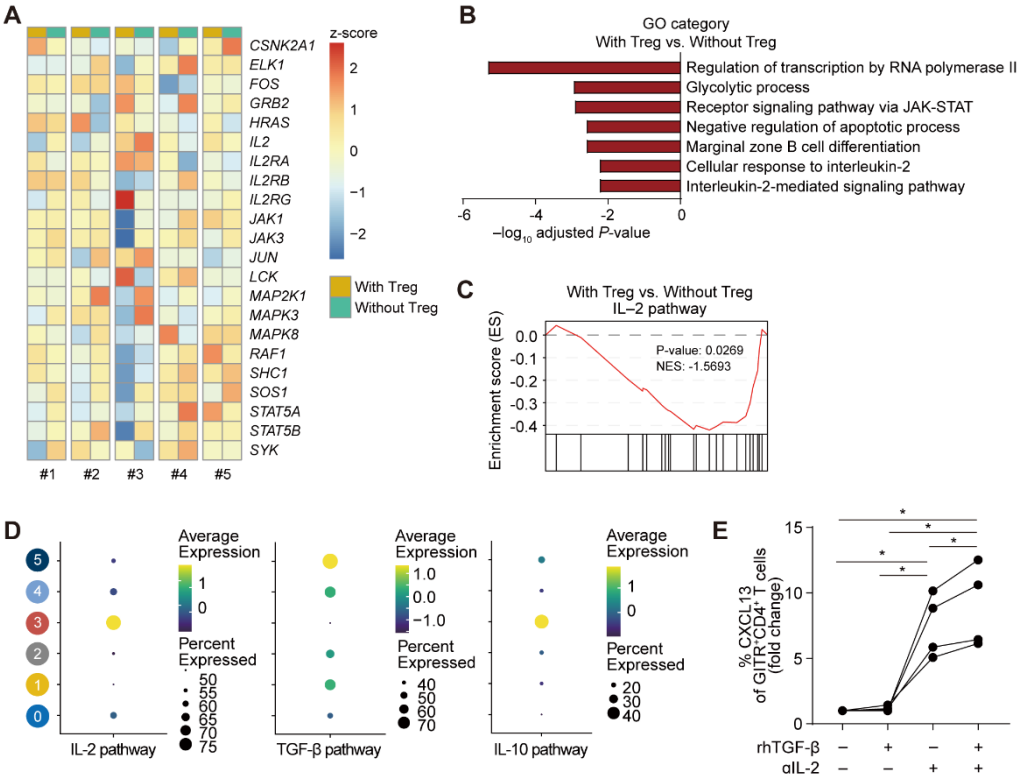

Figure 15. Functional analysis of CXCL13$^+$CD4$^+$ T cells. (A) Heatmap showing BioCarta IL-2 pathway in with versus without Tregs condition. (B) Gene ontology analysis using downregulated DEGs and (C) gene set enrichment analysis of IL-2 pathway gene signatures from the bulk RNA-Seq of CD4$^+$ T cells in the Treg-undepleted condition compared with the Treg-depleted condition (n = 5). (D) Dot plot showing expression of genes involved in the IL-2 pathway, TGF-β pathway, and IL-10 pathway in each cluster, as assessed by scRNA-Seq. (E) CXCL13$^+$CD4$^+$ T cells were differentiated in the presence or absence of neutralizing anti–IL-2 antibody and/or TGF-β. Relative frequencies of CXCL13$^+$ cells in GITR$^+$CD4$^+$ T cells (n = 5). Paired t tests were used to compare values for 2-variable plots. *$P < 0.05$.

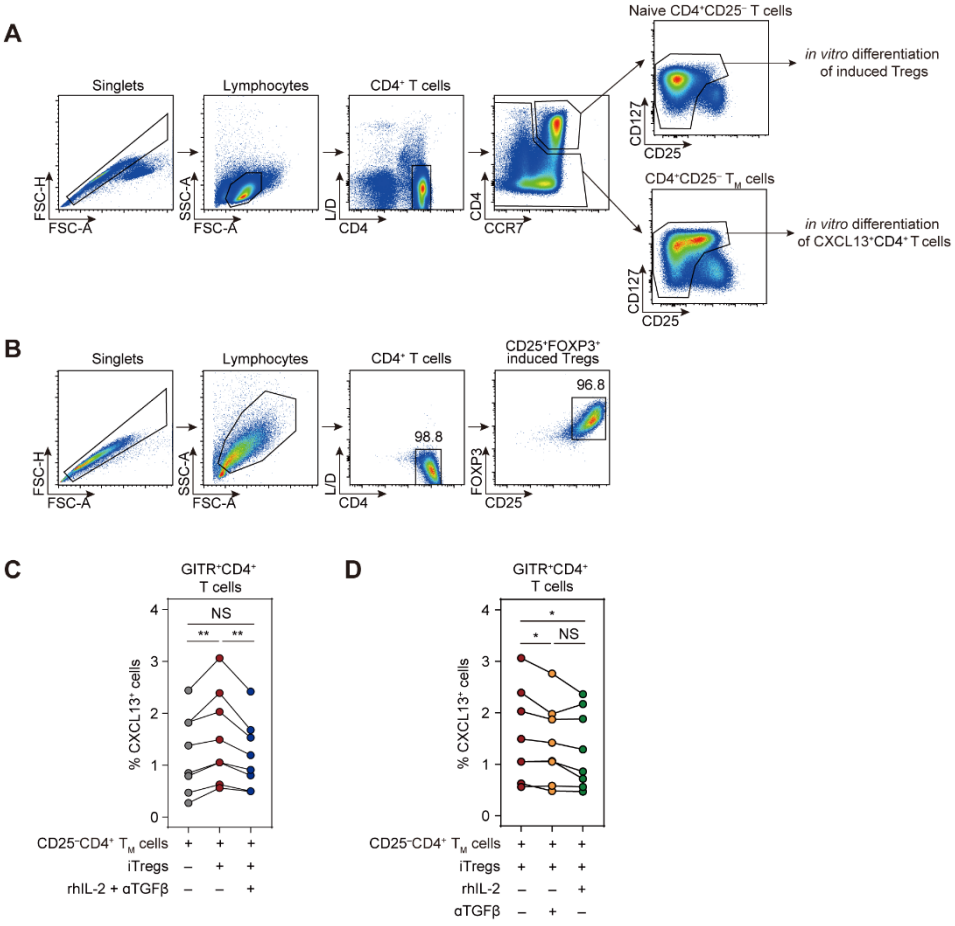

Figure 16. In vitro coculture of induced Tregs (iTregs) and CXCL13^{+}CD4^{+} T cells. (A and B) Gating strategy for flow cytometric analysis of in vitro differentiation of CXCL13^{+}CD4^{+} T cells (A) and induced Treg (B) for co-culture system. (C and D) Differentiated CXCL13^{+}CD4^{+} T cells were cocultured with or without induced Tregs the in presence or absence recombinant IL-2 protein and TGF-β–blocking antibody. Relative frequencies of CXCL13^{+} cells in GITR^{+}CD25$^{-/lo}$CD4^{+} T cells (n = 8). Paired t tests were used to compare values for 2-variable plots. $^{**}P < 0.005$.

3.10. Intralesional corticosteroid injection effectively controls chronic blistering with skin TLSs in patients with pemphigus.

We treated 18 patients with skin TLSs with intralesional corticosteroid injection (ILI). All lesions were reduced after treatment, and 5 of the lesions achieved complete clearance after ILI (**Figure 17A**). We observed the disappearance of TLSs in the removed lesion (**Figure 17B**). We obtained bulk RNA-Seq data for skin lesions with TLSs from 3 patients before and after ILI treatment and found that *CXCL13* was downregulated after treatment (**Figure 17C**). The top 10 TCR clones in lesions disappeared after ILI treatment (**Figure 17D**). Taken together, these results demonstrate that intralesional treatment with corticosteroids improves chronic blisters in pemphigus and reduces cutaneous TLSs.

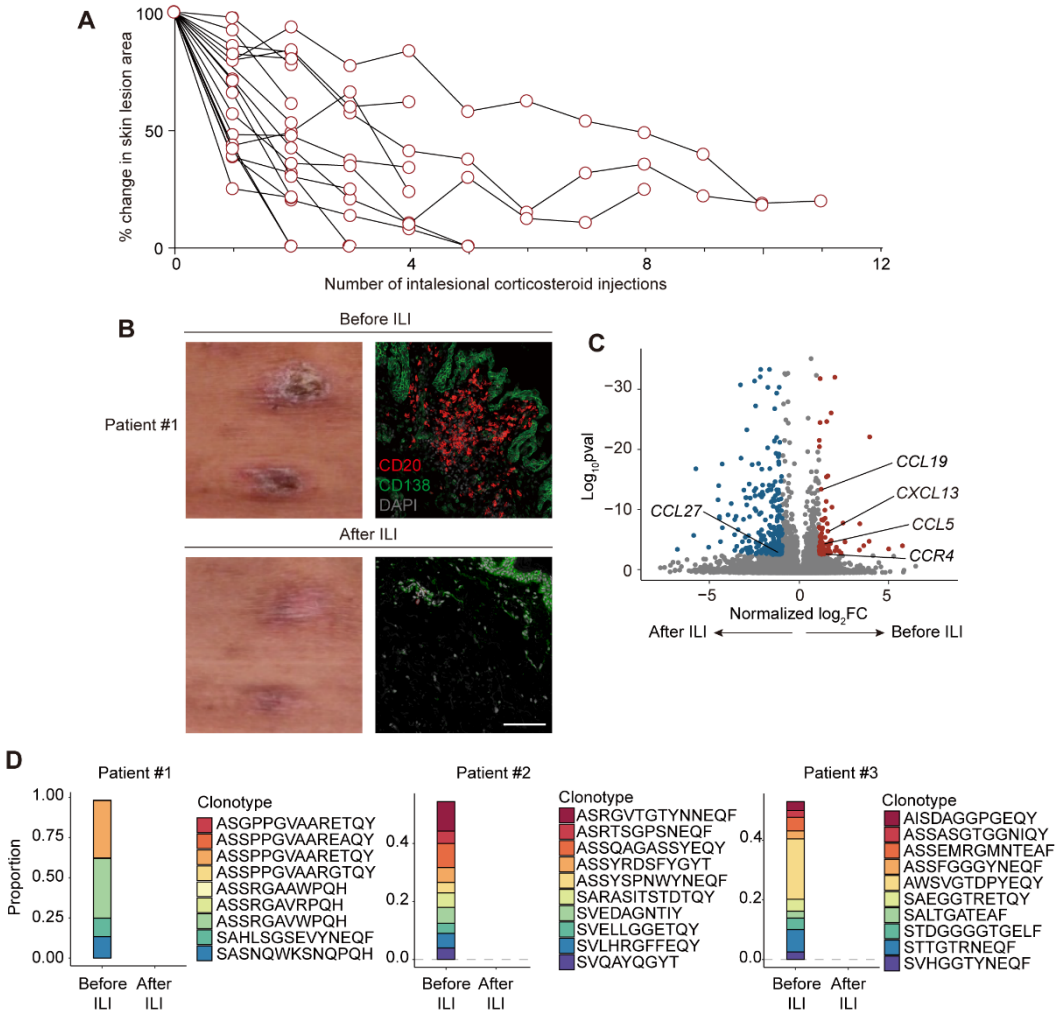

Figure 17. Intralesional corticosteroid injection ameliorates chronic blisters with skin TLSs in patients with pemphigus. (A) Change in skin lesion areas during Intralesional corticosteroid injection (ILI) in 18 patients. (B) Representative clinical images and immunofluorescence staining of a tertiary lymphoid structure–positive (TLS-positive) chronic lesion in patient 1 before and after ILI. Tissues were costained with CD20 (red), CD138 (green), and DAPI (light gray). Scale bar: 100 μm. (C and D) Bulk RNA-Seq of paired skin lesions with TLSs for comparison of before and after ILI (n = 3). (C) Volcano plot shows upregulated (red dots) and downregulated DEGs (blue dots). (D) Bulk TCR-Seq of paired skin lesions with TLSs for the

comparison of before and after ILI (patient #1 to #3). The change in the proportion of top 10 clones of the TCRβ chains is shown for each patient.

4. DISCUSSION

The role of TLSs in the pathogenesis of pemphigus remains unknown, although TLSs have been detected in inflamed lesions in patients with pemphigus[28, 29]. In this study, we showed local pathogenicity of skin TLSs in pemphigus. We observed that DSG-specific B cells and plasma cells colocalize in skin TLSs, suggesting that plasma cells that differentiate from DSG-specific B cells in TLSs produce pathogenic autoantibodies that contribute to suprabasal acantholytic blisters. Furthermore, our findings provide important evidence of the need for local treatment of chronic lesions in pemphigus, though the current treatment guidelines for pemphigus focus on systemic approaches based on the pathomechanism of B cell autoimmunity.

Given that mature TLSs provide an inflammatory antitumor environment and contribute to peripheral tissue autoimmunity[21, 30, 31], identification of factors that can control TLSs is crucial for treatment not only of cancers, but also autoimmune diseases. As CXCL13 is sufficient to induce TLSs[25, 26], it is important to understand the expansion and regulation of CXCL13-expressing cells in TLSs. $CXCL13^+$ T cells in inflamed human tissues have various phenotypes depending on the disease[32, 33]. In rheumatoid arthritis, CXCL13 is highly produced by $PD\text{-}1^{hi}CXCR5^-CD4^+$ T cells in the synovium, which are different from Tfh cells[32]. In malignancies, $CXCL13^+CD4^+$ T cells demonstrate high expression of *IFNG*, *GZMB*, and *PDCD1*[33]. Moreover, $PD\text{-}1^{hi}CXCL13^+CD8^+$ T cells have been detected in several cancers[34, 35]. Consistent with these data, we observed that approximately 90% of $CXCL13^+CD4^+$ T cells in skin TLSs in pemphigus are $PD\text{-}1^+$ cells. Furthermore, although demonstrated in only one sample, the activated $CXCL13^+CD4^+$ T cells include DSG-specific $CD4^+$ T cells. Taken together, these data suggest that TCR stimulation may initially promotes the clonal expansion of $CXCL13^+CD4^+$ T cells.

Tregs have classically been recognized to suppress inflammation, but recent studies have shown that Tregs located in nonlymphoid tissues have functional diversity beyond immunosuppression[36]. In terms of conventional Tfh cells, Tregs restrict their expansion mediated by CTLA-4[37, 38]. However, we observed paradoxical attenuation of genes associated with TCR signaling in $CD4^+$ T cells expressing high levels of CXCL13, indicating that antigens are not necessary for high production of CXCL13 in $CD4^+$ T cells within TLSs. Our results showed that Tregs spatially adjacent to $CXCL13^+CD4^+$ T cells and induce CXCL13 expression in $CD4^+$ T cells. Furthermore, in agreement with previous studies[27, 39], we have shown that TGF-β and anti–IL-2–blocking antibody induce $CXCL13^+CD4^+$ T cells. TGF-β, especially, is known to enhance CXCL13 production in $CD4^+$ T cells by increasing *SOX4* and repressing *SATB1*[27, 39]. These data indicate the involvement of adjacent Tregs in the regulation of $CXCL13^+CD4^+$ T cells. Therefore, we suggest that Tregs play an important role in enhancing the secretion of CXCL13 in preexpanded clonal $CD4^+$ T cells.

In the present study, the scalp was the most common site where skin TLSs were present, and skin TLSs, specifically B cell–enriched structures, were primarily located adjacent to hair follicles. Immune cells, including dendritic cells, various T cell subsets, and Tregs, have been known to be localized especially near hair follicles in the skin[40, 41], and hair follicles attract immune cells when under mechanical stress[42]. This inflammation can occur during chronic autoimmune responses in the skin. Indeed, proinflammatory cytokines such as IL-6 and TNF-α also contribute to the generation of $CXCL13^{+}CD4^{+}$ T cells[27]. Although $CXCL13^{+}CD4^{+}$ T cells may comprise a heterogeneous population of cells[43], our scRNA-Seq analysis revealed that the Th1-like Trm cell feature was prominently detected in these cells. Given that chronic lesions with skin TLSs tend to be persistent, $CXCL13^{+}CD4^{+}$ T cells, which possess skin-resident features, can potentially contribute to long-lasting blisters. It is possible that this characteristic is influenced by microenvironmental factors, such as IL-7 and IL-15, which are produced by the hair follicle[44]. Taken together, preferential involvement of the scalp for skin TLSs may be due to the microenvironment promoted by high hair density. Though this study we conclude that skin TLSs are associated with the persistence of chronically recurrent blisters in patients with pemphigus, and the microenvironmental network involving $CXCL13^{+}CD4^{+}$ T cells and Tregs within these structures plays an important role in CXCL13 production.

5. CONCLUSION

Our study showed the pathogenicity of skin TLSs and introduces a local therapeutic approach for controlling chronic lesions in pemphigus. Our approach provides critical insights by using scRNA-seq and scTCR-seq data coupled with highly multiplex imaging techniques into the expansion and activation of $CXCL13^{+}CD4^{+}$ T cells as important drivers of TLS formation. These findings may contribute to understanding the development of TLSs in other diseases, including cancers as well as autoimmune diseases.

References

1. Kasperkiewicz M, Ellebrecht CT, Takahashi H, Yamagami J, Zillikens D, Payne AS, et al. Pemphigus. *Nat Rev Dis Primers.* 2017;3.
2. Kim JH, and Kim SC. Paraneoplastic Pemphigus: Paraneoplastic Autoimmune Disease of the Skin and Mucosa. *Front Immunol.* 2019;10.
3. Payne AS, Ishii K, Kacir S, Lin CY, Li H, Hanakawa Y, et al. Genetic and functional characterization of human pemphigus vulgaris monoclonal autoantibodies isolated by phage display. *J Clin Invest.* 2005;115(4):888-99.
4. Kim JH, Kim YH, Kim MR, and Kim SC. Clinical efficacy of different doses of rituximab in the treatment of pemphigus: a retrospective study of 27 patients. *Brit J Dermatol.* 2011;165(3):646-51.
5. Wang HH, Liu CW, Li YC, and Huang YC. Efficacy of Rituximab for Pemphigus: A Systematic Review and Meta-analysis of Different Regimens. *Acta Derm-Venereol.* 2015;95(8):928-32.
6. Song AH, Jang J, Lee AY, Min SY, Lee SG, Kim SC, et al. Clinical impact and a prognostic marker of early rituximab treatment after rituximab reimbursement in Korean pemphigus patients. *Front Immunol.* 2022;13.
7. Song A, Lee SE, and Kim JH. Review Article Immunopathology and Immunotherapy of Inflammatory Skin Diseases. *Immune Netw.* 2022;22(1).
8. Schumacher TN, and Thommen DS. Tertiary lymphoid structures in cancer. *Science.* 2022;375(6576):eabf9419.
9. Pitzalis C, Jones GW, Bombardieri M, and Jones SA. Ectopic lymphoid-like structures in infection, cancer and autoimmunity. *Nat Rev Immunol.* 2014;14(7):447-62.
10. Cabrita R, Lauss M, Sanna A, Donia M, Skaarup Larsen M, Mitra S, et al. Tertiary lymphoid structures improve immunotherapy and survival in melanoma. *Nature.* 2020;577(7791):561-5.
11. Helmink BA, Reddy SM, Gao J, Zhang S, Basar R, Thakur R, et al. B cells and tertiary lymphoid structures promote immunotherapy response. *Nature.* 2020;577(7791):549-55.
12. Petitprez F, de Reyniès A, Keung EZ, Chen TW, Sun CM, Calderaro J, et al. B cells are associated with survival and immunotherapy response in sarcoma. *Nature.*

2020;577(7791):556-60.

13. Armengol MP, Juan M, Lucas-Martín A, Fernández-Figueras MT, Jaraquemada D, Gallart T, et al. Thyroid autoimmune disease: demonstration of thyroid antigen-specific B cells and recombination-activating gene expression in chemokine-containing active intrathyroidal germinal centers. *Am J Pathol.* 2001;159(3):861-73.
14. Humby F, Bombardieri M, Manzo A, Kelly S, Blades MC, Kirkham B, et al. Ectopic lymphoid structures support ongoing production of class-switched autoantibodies in rheumatoid synovium. *PLoS Med.* 2009;6(1):e1.
15. Salomonsson S, Jonsson MV, Skarstein K, Brokstad KA, Hjelmström P, Wahren-Herlenius M, et al. Cellular basis of ectopic germinal center formation and autoantibody production in the target organ of patients with Sjogren's syndrome. *Arthritis Rheum-Us.* 2003;48(11):3187-201.
16. Sims GP, Shiono H, Willcox N, and Stott DI. Somatic hypermutation and selection of B cells in thymic germinal centers responding to acetylcholine receptor in myasthenia gravis. *Journal of Immunology.* 2001;167(4):1935-44.
17. Aloisi F, and Pujol-Borrell R. Lymphoid neogenesis in chronic inflammatory diseases. *Nat Rev Immunol.* 2006;6(3):205-17.
18. Rao DA. T Cells That Help B Cells in Chronically Inflamed Tissues. *Front Immunol.* 2018;9:1924.
19. Gu-Trantien C, Migliori E, Buisseret L, de Wind A, Brohée S, Garaud S, et al. CXCL13-producing TFH cells link immune suppression and adaptive memory in human breast cancer. *JCI Insight.* 2017;2(11).
20. Zhang Y, Chen H, Mo H, Hu X, Gao R, Zhao Y, et al. Single-cell analyses reveal key immune cell subsets associated with response to PD-L1 blockade in triple-negative breast cancer. *Cancer Cell.* 2021;39(12):1578-93.e8.
21. Sautès-Fridman C, Petitprez F, Calderaro J, and Fridman WH. Tertiary lymphoid structures in the era of cancer immunotherapy. *Nat Rev Cancer.* 2019;19(6):307-25.
22. Kim SH, Oh J, Roh WS, Park J, Chung KB, Lee GH, et al. Pellino-1 promotes intrinsic activation of skin-resident IL-17A-producing T cells in psoriasis. *J Allergy Clin Immunol.* 2023;151(5):1317-28.
23. Black S, Phillips D, Hickey JW, Kennedy-Darling J, Venkataraaman VG, Samusik N, et al.

CODEX multiplexed tissue imaging with DNA-conjugated antibodies. *Nat Protoc.* 2021;16(8):3802-+.

24. Greenwald NF, Miller G, Moen E, Kong A, Kagel A, Dougherty T, et al. Whole-cell segmentation of tissue images with human-level performance using large-scale data annotation and deep learning. *Nat Biotechnol.* 2022;40(4):555-+.
25. Luther SA, Lopez T, Bai W, Hanahan D, and Cyster JG. BLC expression in pancreatic islets causes B cell recruitment and lymphotoxin-dependent lymphoid neogenesis. *Immunity.* 2000;12(5):471-81.
26. Marchesi F, Martin AP, Thirunarayanan N, Devany E, Mayer L, Grisotto MG, et al. CXCL13 expression in the gut promotes accumulation of IL-22-producing lymphoid tissue-inducer cells, and formation of isolated lymphoid follicles. *Mucosal Immunol.* 2009;2(6):486-94.
27. Yoshitomi H, Kobayashi S, Miyagawa-Hayashino A, Okahata A, Doi K, Nishitani K, et al. Human Sox4 facilitates the development of CXCL13-producing helper T cells in inflammatory environments. *Nat Commun.* 2018;9(1):3762.
28. Yuan HJ, Zhou SR, Liu ZC, Cong WT, Fei XC, Zeng WH, et al. Pivotal Role of Lesional and Perilesional T/B Lymphocytes in Pemphigus Pathogenesis. *J Invest Dermatol.* 2017;137(11):2362-70.
29. Lee AY, Kim T, and Kim JH. Understanding CD4(+) T cells in autoimmune bullous diseases. *Front Immunol.* 2023;14.
30. Sharonov GV, Serebrovskaya EO, Yuzhakova DV, Britanova OV, and Chudakov DM. B cells, plasma cells and antibody repertoires in the tumour microenvironment. *Nat Rev Immunol.* 2020;20(5):294-307.
31. Bombardieri M, Lewis M, and Pitzalis C. Ectopic lymphoid neogenesis in rheumatic autoimmune diseases. *Nat Rev Rheumatol.* 2017;13(3):141-54.
32. Rao DA, Gurish MF, Marshall JL, Slowikowski K, Fonseka CY, Liu Y, et al. Pathologically expanded peripheral T helper cell subset drives B cells in rheumatoid arthritis. *Nature.* 2017;542(7639):110-4.
33. Ren X, Zhang L, Zhang Y, Li Z, Siemers N, and Zhang Z. Insights Gained from Single-Cell Analysis of Immune Cells in the Tumor Microenvironment. *Annu Rev Immunol.* 2021;39:583-609.

34. Savas P, Virassamy B, Ye C, Salim A, Mintoff CP, Caramia F, et al. Single-cell profiling of breast cancer T cells reveals a tissue-resident memory subset associated with improved prognosis. *Nat Med.* 2018;24(7):986-93.
35. Li H, van der Leun AM, Yofe I, Lubling Y, Gelbard-Solodkin D, van Akkooi ACJ, et al. Dysfunctional CD8 T Cells Form a Proliferative, Dynamically Regulated Compartment within Human Melanoma. *Cell.* 2019;176(4):775-89.e18.
36. Muñoz-Rojas AR, and Mathis D. Tissue regulatory T cells: regulatory chameleons. *Nat Rev Immunol.* 2021;21(9):597-611.
37. Wing JB, Ise W, Kurosaki T, and Sakaguchi S. Regulatory T cells control antigen-specific expansion of Tfh cell number and humoral immune responses via the coreceptor CTLA-4. *Immunity.* 2014;41(6):1013-25.
38. Sage PT, Paterson AM, Lovitch SB, and Sharpe AH. The coinhibitory receptor CTLA-4 controls B cell responses by modulating T follicular helper, T follicular regulatory, and T regulatory cells. *Immunity.* 2014;41(6):1026-39.
39. Chaurio RA, Anadon CM, Lee Costich T, Payne KK, Biswas S, Harro CM, et al. TGF-β-mediated silencing of genomic organizer SATB1 promotes Tfh cell differentiation and formation of intra-tumoral tertiary lymphoid structures. *Immunity.* 2022;55(1):115-28.e9.
40. Sanchez Rodriguez R, Pauli ML, Neuhaus IM, Yu SS, Arron ST, Harris HW, et al. Memory regulatory T cells reside in human skin. *J Clin Invest.* 2014;124(3):1027-36.
41. Kobayashi T, Naik S, and Nagao K. Choreographing Immunity in the Skin Epithelial Barrier. *Immunity.* 2019;50(3):552-65.
42. Nagao K, Kobayashi T, Moro K, Ohyama M, Adachi T, Kitashima DY, et al. Stress-induced production of chemokines by hair follicles regulates the trafficking of dendritic cells in skin. *Nat Immunol.* 2012;13(8):744-52.
43. Kobayashi S, Murata K, Shibuya H, Morita M, Ishikawa M, Furu M, et al. A Distinct Human CD4+T Cell Subset That Secretes CXCL13 in Rheumatoid Synovium. *Arthritis Rheum-Us.* 2013;65(12):3063-72.
44. Adachi T, Kobayashi T, Sugihara E, Yamada T, Ikuta K, Pittaluga S, et al. Hair follicle-derived IL-7 and IL-15 mediate skin-resident memory T cell homeostasis and lymphoma. *Nature Medicine.* 2015;21(11):1272-9.

Abstract in Korean

천포창 환자의 만성 병변에서 삼차 림프양 구조의 병인성 역할 규명

본 논문은 천포창이라는 자가면역 수포성 질환의 만성 병변에서 발견된 삼차 림프양 구조가 질환의 병인성에 중요한 역할을 한다는 사실을 규명하였다. 천포창은 데스모글레인 1 과 3 단백에 대한 자가항체 생성으로 인해 피부 및 점막 표피에서 가시세포 분리가 발생하여 전신에 수포를 유발하는 희귀하고 치명적인 자가면역 수포성 질환으로, 심각한 경우 사망에 이를 수도 있다. 이러한 천포창 환자를 치료하기 위해서 현재 리툭시맙과 고용량 전신 코르티코스테로이드 및 면역억제제를 사용하는 약물 치료에도 불구하고, 일부 환자에서 수 개월 이상 만성적으로 지속되는 피부 병변을 관찰하였다. 천포창 환자의 만성 피부 병변에서 병원성 항체를 생성하는 데스모글레인 특이적인 B 세포와 형질 세포가 삼차 림프양 구조 내에 존재하고 있음을 발견하였다. 이러한 삼차 림프양 구조는 다양한 염증성 질환에서 발견된 바 있으나 아직 천포창 환자의 피부 병변에 존재하는 삼차 림프양 구조의 역할은 제대로 밝혀진 바 없다. 본 연구에서는 삼차 림프양 구조에서 CXCL13 을 주로 분비하는 세포가 CD4 T 세포임을 확인하였으며, 최근 고도화된 단일 세포 유전체 분석 및 공간 다중체 분석을 활용하여, 삼차 림프양 구조 내에서 $CXCL13^{+}CD4^{+}$ T 세포의 특징을 높은 해상도로 면밀하게 관찰하였다. $CXCL13^{+}CD4^{+}$ T 세포는 데스모글레인 특이적인 T 세포를 포함하고 있으면서, Th1-like cytotoxic 하게 활성화되어 있는 특징을 나타냈으며, 주변에 인접해 있는 조절 T 세포에 의해서 CXCL13 생산을 분비하고 조절될 수 있음을 확인하였다. 이를 생체 외 실험을 통해 조절 T 세포를 제거하면 CXCL13 생산이 감소함을 확인함으로써 삼차 림프양 구조의 미세환경을 형성하고 조절하는데 중요한 세포임을 확인하였다. 이러한 천포창 환자의 만성 병변에 국소 스테로이드를 주사하여 치료하였더니 오랫동안 낫지 않았던 만성 병변이 효과적으로 개선될 수 있음을 실험적으로 입증함으로써 천포창 환자의 만성 병변을 치료할 수 있는 새로운 치료 전략을 제시하였다. 본 연구 결과는 천포창의 병인에 대한 중요한 통찰력을 제공하며 자가면역질환에 대한 이해를 높이고 새로운 치료 전략을 개발하는 데 기여할 것으로 기대된다.

핵심되는 말 : 천포창, 자가면역 수포성 질환, 삼차 림프양 구조, 만성 병변, 병인성, 리툭시맙, $CD4^{+}$ T 세포, B 세포

PUBLICATION LIST

Han D, **Lee AY**, Kim T, Choi JY, Cho MY, Song A, Kim C, Shim JH, Kim HJ, Kim H, Blaize D'Angio H, Preska R, Mayer AT, Kim M, Choi EJ, Kim TG, Shin EC, Park K, Kim D, Kim SC, Kim JH. Microenvironmental network of clonal $CXCL13^{+}CD4^{+}$ T cells and regulatory T cells in pemphigus chronic blisters. *J Clin Invest*. 2023 Dec;133(23): e166357

Lee AY, Kim T, Kim JH. Understanding $CD4^{+}$ T cells in autoimmune bullous diseases. *Front Immunol*. 2023 Apr;14:1161927

Song A, Jang J, **Lee A**, Min SY, Lee SG, Kim SC, Shin J, Kim JH. Clinical impact and a prognostic marker of early rituximab treatment after rituximab reimbursement in Korean pemphigus patients. *Front Immunol*. 2022 Aug;13:932909.